Ocean Engineering 363 (2026) 126575

Contents lists available at ScienceDirect

Ocean Engineering

journal homepage: www.elsevier.com/locate/oceaneng

Research paper

Bio-inspired semi-submersible platform for improving the hydrodynamic stability of floating vertical-axis wind turbines

Kunpeng Liu [a], Haoda Huang [a,b], Qingsong Liu [b,*], Qiang Zhang [a,e], Chun Li [a], Gregorio Iglesias [b,c], Jin Wang [e], Musa Bashir [d]

[a] School of Energy and Power Engineering, University of Shanghai for Science and Technology, Shanghai, 200093, China
[b] School of Engineering and Architecture, University College Cork, T12 K8AF, Ireland
[c] School of Engineering, Computing and Mathematics (SECaM), University of Plymouth, Plymouth, PL48 AA, United Kingdom
[d] School of Engineering, University of Liverpool, The Quadrangle, Brownlow Hill, L69 3GH, United Kingdom
[e] Liverpool Logistics, Offshore and Marine (LOOM) Research Institute, Liverpool John Moores University, Byrom Street, Liverpool, L3 3AF, United Kingdom

ARTICLE INFO

Keywords:
Floating vertical axis wind turbine
Bio-inspired
Computational fluid dynamics
Coupled aero-hydrodynamic analysis
Semi-submersible platform

ABSTRACT

Floating vertical axis wind turbines (VAWTs) offer high power density, directional insensitivity and convenient operation and maintenance; however, their large power fluctuations and limited survivability under extreme sea states hinder utility-scale deployment. To address these challenges, this study proposes a water hyacinth (WH)-inspired semi-submersible platform incorporating biomimetic buoyancy chambers parameterized using Bézier curves. Three configurations (WHS, WHM, and WHL) are developed and evaluated using a Dynamic Fluid-Body Interaction (DFBI) approach coupled with a Volume of Fluid (VOF) model under combined wind-wave loading. The biomimetic geometry modifies the added-mass distribution, hydrodynamic damping, and local flow structures around the platform, leading to reductions of up to 16.3%, 15.5%, and 15.0% in the dominant surge, heave, and pitch responses, respectively. Among the three configurations, WHM exhibits the most balanced hydrodynamic performance. Further comparisons with spherical, cylindrical, and disc-shaped buoyancy structures of equivalent volume demonstrate that the improved stability originates from the biomimetic morphology rather than buoyancy enhancement alone. When integrated into a floating VAWT system, the WHM platform reduces surge, heave, and pitch responses by 0.8%, 11%, and 10%, respectively, while decreasing the power spectral density of the power coefficient by approximately 18.6%. Overall, the proposed WH-inspired platform provides an effective passive strategy for improving the hydrodynamic stability and smoothing power output of floating VAWTs.

1. Introduction

The global energy sector is undergoing a rapid transition toward low-carbon and sustainable development. Among various renewable energy technologies, offshore wind energy has attracted considerable attention because of its abundant resources, high wind speeds, and relatively stable wind conditions (Cao et al., 2025). According to the Global Wind Energy Council (GWEC) 2026 report (GWEC, 2026), a record 164.6 GW of new wind power capacity was installed worldwide in 2025, including 9.3 GW of offshore wind capacity, representing an 18% increase compared with the previous year. As offshore wind farms continue to expand into deeper waters, floating wind technologies are expected to play an increasingly important role in future energy systems.

At present, horizontal-axis wind turbines (HAWTs) dominate the offshore wind industry and have reached a relatively high level of technological maturity (Ullah and Alam, 2026). In contrast, floating vertical-axis wind turbines (FVAWTs) remain at a lower technology readiness level. Nevertheless, recent demonstration projects indicate that floating VAWTs are gradually progressing from conceptual studies toward engineering implementation. The SeaTwirl S1 prototype (NEW ATLAS, 2022), a 30-kW floating VAWT deployed off the Swedish coast, has demonstrated long-term offshore operation and survivability under harsh environmental conditions. More recently, the Horizon Europe funded Verti-Go project was launched to demonstrate a 2 MW floating VAWT system (offshoreWIND, 2025), representing one of the most significant efforts toward the commercial deployment of floating

* Corresponding author.
E-mail address: QLiu@ucc.ie (Q. Liu).

https://doi.org/10.1016/j.oceaneng.2026.126575
Received 16 March 2026; Received in revised form 10 June 2026; Accepted 14 June 2026
Available online 18 June 2026

VAWT technology.

From a structural and hydrodynamic perspective, most floating support concepts originally developed for HAWTs, including spar, semi-submersible, and tension-leg platforms, can be directly adapted for floating VAWT applications (Enterprise, 2022). Among them, semi-submersible platforms are widely regarded as one of the most technically mature and industrially promising solutions because of their distributed buoyancy, relatively low center of gravity, favorable motion characteristics, and compatibility with conventional catenary mooring systems (Ghigo et al., 2024). However, under combined wind and wave excitations, floating platforms often exhibit strongly coupled six-degree-of-freedom (6-DOF) motions, characterized by low-frequency and large-amplitude responses. These motions can reduce the operational stability of the system, amplify mooring line tension fluctuations, and increase the risk of extreme platform responses under severe sea states (Tran and Kim, 2016). Therefore, improving platform stability and suppressing low-frequency motions under harsh sea conditions without significantly increasing structural complexity or cost remains a key challenge in floating wind energy research.

To address these challenges, extensive efforts have been devoted to platform optimization through structural redesign, damping enhancement, and mooring system improvement. In terms of floating body design, researchers have explored various geometric configurations, including tapered columns, asymmetric layouts, and modular buoyancy arrangements, to improve load distribution and motion characteristics. For example, He et al. (2025) employed a Copula-based multi-objective optimization framework to enhance the structural layout of a semi-submersible platform under typhoon conditions, while Saeed et al. (2024) developed a lightweight multi-energy platform using topology optimization to reduce structural weight and improve stiffness in critical load-transfer regions. Li et al. (2022) further proposed a modular semi-submersible platform with a hexagonal symmetric arrangement, achieving improved mechanical balance and reduced pitch-roll coupling under multidirectional wave conditions.

Besides geometric optimization, considerable attention has been devoted to passive damping technologies that increase hydrodynamic energy dissipation. Typical approaches include heave plates, skirt structures, and other flow-control appendages that modify added mass and viscous damping characteristics. Zhao et al. (2025) demonstrated that perforated and hexagonal heave plates could effectively suppress heave and pitch motions through enhanced vortex generation and viscous dissipation. Using a combination of CFD simulations and wave-basin experiments, Li et al. (2025) optimized damping plate geometries by regulating the coupling between added mass and damping effects. Similar improvements were reported by Johannesen et al. (Johannesen, 2024), who introduced radial damping structures around the platform to mitigate heave and pitch responses. In addition to purely passive devices, Lin et al. (2025) integrated a Sharp-Eagle wave energy converter array with a DeepCWind floating wind turbine, creating a hybrid wind-wave energy system that simultaneously enhanced energy extraction and platform stability.

Active control strategies have also emerged as an effective means of mitigating platform motions. Existing studies mainly focus on pitch regulation, tower feedback control, and adaptive response management under stochastic environmental loads. Hou et al. (2025) developed a stochastic model predictive control (SMPC) framework capable of reducing both power fluctuations and platform motions under random wind-wave conditions. López-Queija et al. (2024) combined nonlinear model predictive control with a random-walk Monte Carlo algorithm to adaptively tune control parameters, thereby reducing fatigue loads and tower-top motions while maintaining stable power production. Similarly, Liao et al. (2025) proposed a data-driven adaptive control strategy based on random forest and multi-objective optimization, achieving effective suppression of platform drift and improved operational stability. Despite their promising performance, the practical application of these methods is still constrained by sensor dependence, controller complexity, and limited effective frequency bandwidth.

As an essential boundary constraint system, mooring lines play a critical role in maintaining platform stability and suppressing low-frequency motions. A variety of advanced mooring concepts have been proposed to enhance motion control performance. Tian et al. (Tian, 2025) introduced shape memory alloy components into mooring damping systems, enabling adaptive energy dissipation and reducing fatigue damage under cyclic loading. Cruz et al. (2024) investigated synthetic fiber moorings as an alternative to traditional steel chains, demonstrating improved corrosion resistance, flexibility, and weight efficiency. Lin et al. (Lin and Yang, 2023) further proposed a hybrid mooring system combining chains and synthetic fiber ropes, which effectively reduced tension fluctuations, fatigue damage, and platform drift under severe sea states. For deployment in intermediate water depths, Han et al. (2017) developed a semi-tension-leg platform (STLP) concept, in which pre-tensioned vertical tendons provide additional lateral stiffness while maintaining favorable towing and installation characteristics.

Despite these advances, existing studies have predominantly focused on floating HAWTs, while platform concepts specifically designed for floating VAWTs remain relatively limited. Current stabilization strategies mainly rely on geometric modifications, damping devices, active control systems, and mooring innovations to increase restoring forces or dissipate wave energy. Although these approaches can effectively mitigate platform motions, they often increase structural complexity and cost. More importantly, the potential of biomimetic geometries to regulate local flow structures and improve platform stability through passive hydrodynamic mechanisms remains largely unexplored. Nature provides valuable inspiration for such developments. Among aquatic plants, Pontederia crassipes (water hyacinth, WH) exhibits remarkable floating stability owing to the bulbous buoyant organs located at the base of its petioles, as shown in Fig. 1. These air-filled structures provide distributed buoyancy and help maintain a stable posture under continuous wind and wave disturbances (Yang et al., 2025). Such a combination of buoyancy regulation and passive stabilization offers a promising biomimetic concept for floating platform design. It should be noted that the present study adopts a morphology-inspired biomimetic strategy, in which the geometric characteristics of the water hyacinth bladder are transferred to an engineering-scale platform, rather than attempting to reproduce the Reynolds-number-dependent flow physics of the biological prototype.

Inspired by the buoyant morphology of water hyacinth, this study proposes a biomimetic semi-submersible platform in which streamlined buoyancy chambers are integrated into the platform bracing members. Unlike conventional buoyancy enhancement approaches that primarily increase displacement volume, the proposed design aims to modify local flow structures, redistribute buoyancy, and enhance hydrodynamic damping through biomimetic geometry. Three biomimetic configurations with different buoyancy chamber scales are developed and systematically evaluated. In addition, three conventional buoyancy structures, namely spherical, cylindrical, and disc-shaped configurations, are introduced as benchmark cases to assess the effectiveness of the proposed biomimetic concept and to distinguish the influence of

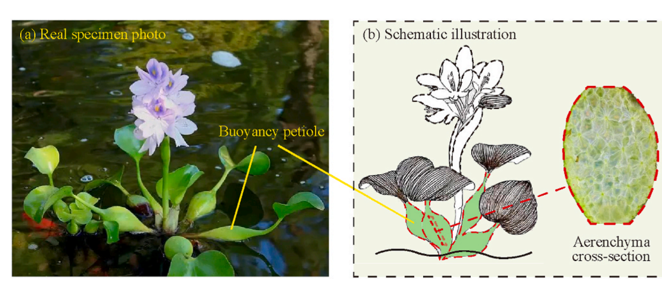

Fig. 1. Morphological features of water hyacinth and its buoyant petiole.

geometric morphology from that of buoyancy enhancement alone.

To investigate the effectiveness of the proposed concept, a fully coupled numerical framework is established in STAR-CCM + using the Dynamic Fluid Body Interaction (DFBI) method. The hydrodynamic responses of different biomimetic platforms are first evaluated in terms of 6-DOF motions, mooring line tensions, and local flow-field characteristics under regular wave conditions. Subsequently, the optimal biomimetic configuration is quantitatively compared with spherical, cylindrical, and disc-shaped buoyancy structures possessing equivalent buoyancy capacity and platform displacement, in order to isolate the effect of geometric morphology on platform performance. The underlying stabilization mechanisms are then analyzed from the perspectives of added-mass effects, vortex evolution, and pressure distribution. Finally, the optimal biomimetic configuration is integrated with a floating VAWT system to assess its influence on coupled aero-hydrodynamic performance. The findings are expected to provide design guidance for passive stabilization strategies and the development of next-generation floating VAWT platforms.

2. Methodology

2.1. DFBI module

The Dynamic Fluid Body Interaction (DFBI) model in STAR-CCM+ is employed to predict the 6-DOF motions of floating VAWTs under combined wind and wave loading. In the absence of external constraints, a rigid body is allowed to move freely in all translational and rotational directions. Its dynamic behavior is determined by solving the equations governing the translational and rotational motions of the center of mass. Based on the global coordinate system, the multibody dynamic equation of motion can be expressed as (Siemens Digital Industries Software, 2025):

$$\mathbf{M}\ddot{\mathbf{q}} = \mathbf{f} \tag{1}$$

where $\mathbf{q}$ is the generalized coordinate vector, $\mathbf{f}$ is the generalized force, and $\mathbf{M}$ is the inertia matrix. The multibody system inertia matrix can be extended from the free motion of a single body, and is defined as follows:

$$\mathbf{M} = \begin{pmatrix} \mathbf{M}_1 & \cdots & 0 \\ \vdots & \ddots & \vdots \\ 0 & \cdots & \mathbf{M}_n \end{pmatrix} \tag{2}$$

If certain degrees of freedom of some rigid bodies are constrained, the governing equations must be solved together with the corresponding constraint equations. The constraint conditions can be expressed as:

$$\phi(\mathbf{q}, \mathrm{t}) = 0 \tag{3}$$

By taking the second derivative of Eq. (3), the linear constraint conditions that the system's acceleration must satisfy can be obtained:

$$\mathbf{J}\ddot{\mathbf{q}} = \mathbf{Q} \tag{4}$$

where $\mathbf{J}$ is the Jacobian matrix of the constraint equations with respect to the generalized coordinates, $\ddot{\mathbf{q}}$ is the generalized acceleration of the system, and $\mathbf{Q}$ is the transpose of the Jacobian matrix associated with the constraint forces.

To incorporate the constraint forces associated with these conditions into the dynamic equations, a Lagrange multiplier $\boldsymbol{\lambda}$ is introduced, and the corresponding constraint reaction forces are formulated as:

$$\mathbf{f}^C = \mathbf{J}^{\mathrm{T}} \cdot \boldsymbol{\lambda} \tag{5}$$

Finally, the total system force $\mathbf{f}$ should include fluid loads, gravity, buoyancy, frictional resistance, and the constraint reaction force $\mathbf{f}^C$. By solving the coupled Eqs. (1)–(5), the instantaneous displacement, velocity, and acceleration of each component of the FOWT can be obtained, thereby providing a complete description of its six-DOF response process.

2.2. VOF multiphase model

To capture the evolution of the air-water interface under wave excitation, the Volume of Fluid (VOF) method is adopted. The VOF model is widely used in marine engineering because of its high interface-capturing accuracy and relatively low computational cost. In this approach, air and water are treated as two immiscible phases, and the free surface is identified through the volume fraction of each phase within the computational cells.

In STAR-CCM+, the VOF model is solved using a single set of governing equations shared by both phases. The interface evolution is tracked through the transport equation of the volume fraction, which can be expressed as (Siemens Digital Industries Software, 2025):

$$\frac{\partial}{\partial t}\int_V \alpha_i \rho_i dV + \oint_V \alpha_i \rho_i \mathbf{v_i} \cdot d\mathbf{a} = \int_V \sum\nolimits_{j \neq i} \left(m_{ij} - m_{ji}\right) dV + \int_V S_i^{\alpha} dV \tag{6}$$

where α_i is the volume fraction, ρ_i is the density, $\mathbf{v_i}$ is the velocity vector, m_{ij} is the mass transfer rate from phase j to phase i, m_{ji} is the mass transfer rate from phase i to phase j, and S_i^{α} is the mass source term.

Combined with the momentum conservation equation, the volume fraction transport equation enables accurate tracking of the free-surface evolution during wave propagation and platform motions. Since no phase mixing or phase change is involved, the VOF model is particularly suitable for simulating the interaction between regular waves and floating platforms. Therefore, it is adopted in this study to model the wave-platform interaction.

2.3. Mooring line model

The mooring system provides the primary restoring force that maintains the position and stability of the floating VAWT. In STAR-CCM+, the mooring lines are modeled using the elastic catenary formulation implemented within the DFBI framework. Each mooring line is represented as a flexible cable with finite axial stiffness and self-weight, allowing the nonlinear geometric characteristics and tension responses of the catenary system to be captured. In a local Cartesian coordinate system, the static catenary profile can be expressed as (Siemens Digital Industries Software, 2025):

$$\begin{cases} x = \mathrm{a}u + \mathrm{b}\sinh(u) + \alpha \\ y = \mathrm{a}\cosh(u) + \mathrm{b}\sinh^2(u)/2 + \beta \\ u_1 \le u \le u_2 \\ \mathrm{a} = \mathrm{c}/\lambda_0 g \\ \mathrm{b} = \mathrm{c}\mathrm{a}/DL_{eq} \\ \mathrm{c} = \lambda_0 g L_{eq}/(\sinh(u_2) - \sinh(u_1)) \end{cases} \tag{7}$$

where g is the gravitational acceleration, λ_0 and L_{eq} are the unit mass per length and the relaxed length of the catenary under no-load conditions, respectively; D is the stiffness of the mooring line; and α and β are integral constants that depend on the positions of the two endpoints and the total mass of the catenary. The relationship between the curve parameter u and the inclination angle ϕ of the catenary can be expressed as Eq. (8):

$$\tan\phi = \sinh(u) \tag{8}$$

The parameters u_1 and u_2 represent the positions of the catenary endpoints p_1 and p_2 in the parametric space, as shown in Fig. 2.

The forces $\mathbf{f}_1$ and $\mathbf{f}_2$ acting on the two endpoints of the catenary are directed along the local tangent vectors of the catenary curve at the parameter values u_1 and u_2, respectively. This can be expressed as Eqs. (9) and (10):

$$\begin{cases} \mathbf{f}_{1,x} = c \\ \mathbf{f}_{1,y} = c\sinh(u_1) \end{cases} \tag{9}$$

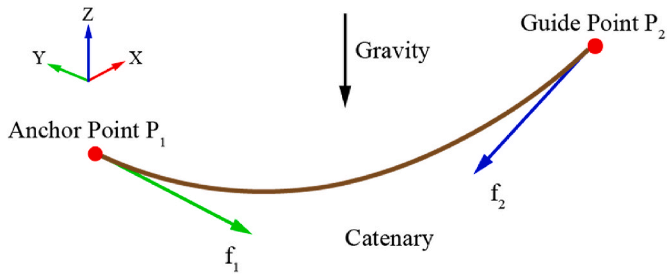

Fig. 2. Mooring system modeling.

$$\begin{cases} \mathbf{f}_{2,x} = -c \\ \mathbf{f}_{2,y} = -c\,\sinh(u_2) \end{cases} \tag{10}$$

2.4. Parametric modeling of WH bladders

To reproduce the distributed buoyancy characteristics of water hyacinth bladders, a parametric modeling method based on Bézier curves (Llamosas-Mayca et al., 2025) is developed. Under a unified arrangement of control points, different bladder configurations are generated by varying the horizontal projection length l and the vertical height h. This approach enables a systematic investigation of the influence of bladder size on platform buoyancy distribution, restoring moments, and hydrodynamic responses. Although slight differences in arc length exist among the generated geometries, all configurations maintain smooth and continuous with consistent curvature characteristics, ensuring the validity of the comparative analysis.

As shown in Fig. 3, the outer profile of the biomimetic bladder is represented using a cubic Bézier curve. The resulting geometry reproduces the characteristic morphology of water hyacinth bladders, featuring a streamlined front section, a bulged middle region, and a tapered tail. Compared with higher-order Bézier curves, the cubic formulation provides sufficient geometric flexibility while maintaining shape consistency and numerical robustness. The mathematical expression of the cubic Bézier curve is given as:

$$B(t) = (1-t)^3 P_0 + 3(1-t)^2 t P_1 + 3(1-t)t^2 P_2 + t^3 P_3, t \in [0,1] \tag{11}$$

where $B(t)$ denotes a point on the bladder contour curve, t is the dimensionless interpolation parameter with a domain of [0, 1], and P_0 to P_3 are the four control points, defined as follows:

$$P_0 = (0,0), P_1 = (x_1, h+\delta), P_2 = (x_2, h+\delta), P_3 = (l, 0) \tag{12}$$

where l is the horizontal projection length of the bladder structure (the distance from the front end to the tail along the horizontal axis), with units of meters; h is the maximum vertical height of the bladder structure (the highest point of the outer contour), also in meters; x_1 is the x-coordinate of the first intermediate control point, which governs the curvature of the front section; x_2 is the x-coordinate of the second intermediate control point, which governs the contraction of the tail section; and δ is the vertical adjustment term used to enhance the bulging effect, typically set to 10-20% of b.

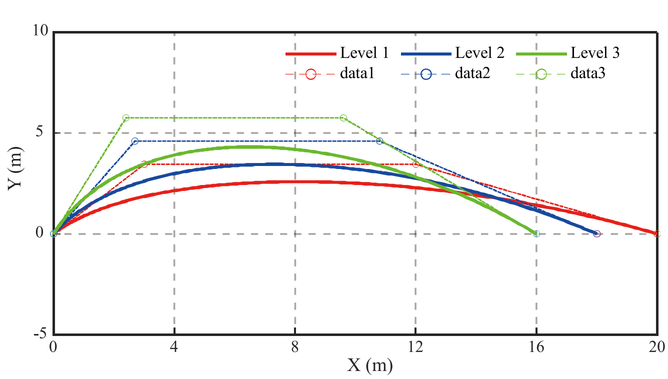

Fig. 3. Size and shape optimization of the WH parametric model.

3. Model establishment

3.1. Floating VAWT

The floating VAWT system analyzed in this study consists of a rotor and tower supported by a semi-submersible platform with a catenary mooring system, as shown in Fig. 4. The rotor adopts a typical H-type configuration, in which three straight blades are evenly spaced and connected to the central shaft through upper and lower arms. The blades employ the DU-06-W-200 airfoil developed by Claessens (2006) specifically for VAWTs application. The airfoil has a thickness ratio of 20% and a camber ratio of 0.8%, providing improved aerodynamic and structural performance compared with conventional symmetric profiles. The main geometric parameters of the floating VAWT are listed in Table 1, and further details on the modeling procedure can be found in author's previous work (Liu et al., 2024).

The platform is based on the OC4-DeepCwind semi-submersible platform developed within Phase II of the Offshore Code Comparison Collaboration Continuation (OC4) project coordinated by the National Renewable Energy Laboratory (NREL) (National Renewable Energy Laboratory, 2014). The platform consists of three main columns, upper and lower ring pontoons, and cross braces arranged in 120° symmetric layout. Each main column has a diameter of 6.5 m, and a center-to-center spacing of 50 m. The platform draft is approximately 20 m, while the upper and lower ballast tanks are filled to water depths of 7.83 m and 5.17 m, respectively, to satisfy hydrostatic equilibrium requirements.

To improve geometric consistency and mesh quality, minor modifications were made to the brace-pontoon connections during model construction. These adjustments have a negligible influence on the global hydrodynamic characteristics of the platform. The mass properties were calculated using ABAQUS and verified against the OC4 reference data. The resulting mass, center of gravity, and moments of inertia show good agreement with the reference values and are summarized in

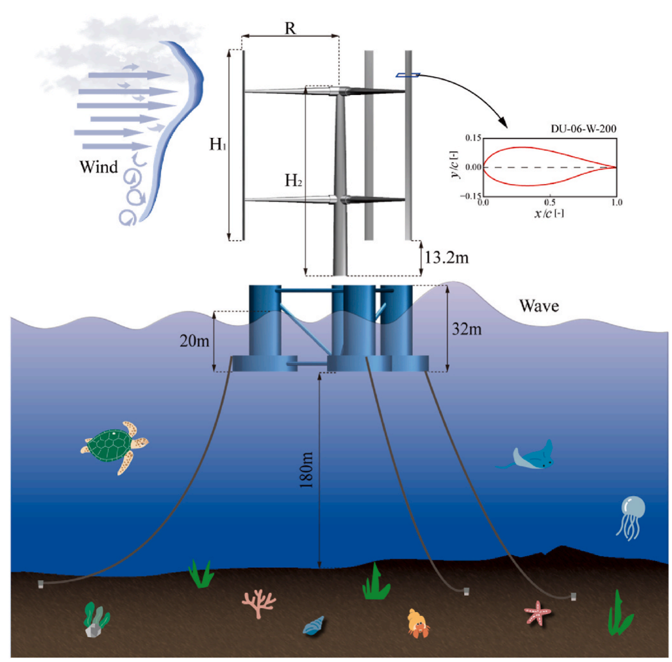

Fig. 4. Geometric model of the floating VAWT.

Table 1
Geometric parameters of the floating VAWT.

Parameter/Unit	Value
Number of Blades	3
Number of Support Rods per Blade	2
Blade Height H_1/m	70.25
Tower Height H_2/m	68.29
Rotor Radius R/m	36.76
Blade Chord Length c/m	3.512
Blade Pitch Angle β/°	2
Rated Rotational Speed ω/rpm	6.81

Table 2
Comparison of mass-related properties of the floating platform with OC4 report.

Structural Parameter/Unit	Value in Ref (National Renewable Energy Laboratory, 2014)	Value in FEM value	Error
Mass (including ballast water)/kg	1.3473×10^7	1.3473×10^7	0.0%
Center of Mass (below waterline)/m	13.46	13.46	0.0%
Roll Moment of Inertia I_{xx}/kg·m^2	6.827×10^9	6.56×10^9	−3.9%
Pitch Moment of Inertia I_{yy}/kg·m^2	6.827×10^9	6.56×10^9	−3.9%
Yaw Moment Of Inertia I_{zz}/kg·m^2	1.226×10^{10}	1.17×10^{10}	−4.6%

Table 2.

The platform is station-kept by three catenary mooring lines arranged symmetrically at 120° intervals, as shown in Fig. 5. Line C2 is aligned with the wave propagation direction, while lines C1 and C3 are positioned symmetrically on either side of the platform. One end of each mooring line is attached to the platform above the lower pontoon, and the other end is anchored to the seabed. The mooring system is modeled using the quasi-static catenary formulation described in Section 2.3, neglecting seabed friction effects. The initial tension and equilibrium profile of each mooring line are obtained from the catenary equations and subsequently applied as boundary constraints in the motion simulations. The submerged mass density of the mooring line is 108.63 kg/m after buoyancy correction. The main material properties of the mooring lines are listed in Table 3.

3.2. Biomimetic platform

Based on the Bézier curve parameterization method described in Section 2.4, Three representative configurations were selected to cover a practical range of chamber scales, namely a slender configuration (WHS, $l/h = 20/3$), an intermediate configuration (WHM, $l/h = 18/4$), and a thick configuration (WHL, $l/h = 16/5$). This arrangement enables a systematic evaluation of the influence of chamber scaling while

Table 3
Mass-related parameters of mooring system.

Structural Parameter/Unit	Value
Relaxation length l_c/m	835.5
Cross-sectional diameter d_c/m	0.0766
Mass density/(kg/m)	113.35
Mass density in water/(kg/m)	108.63
Stiffness/(N/m)	7.536×10^8

preserving the same biomimetic morphology. The buoyancy chambers are installed along the inclined braces of the semisubmersible platform and connected to the main columns. The distance between the bottom of each chamber and the connection point on the main column is fixed at 4 m for all configurations. The resulting three-dimensional models and the corresponding parameters are shown in Fig. 6.

During the modeling process, the WH buoyancy chambers are simplified as shell structures and assigned rigid plastic properties with a density of 1400 kg/m^3 and a Young's modulus of 2×10^9 Pa. The biomimetic platform models were then imported into ABAQUS to determine the mass property, including the total mass, center of gravity, and moments of inertia. These parameters were subsequently used to define the DFBI motion model in STAR-CCM+. The resulting mass properties are summarized in Tables 4 and 5.

As shown in Table 4, the introduction of the WH buoyancy chambers causes only a slight increase in the platform mass without considering ballast water, with all configurations remaining within 1% of the original platform. The centers of gravity and principal moments of inertia also show minimal variation, indicating that the biomimetic chambers have a negligible influence on the overall inertial characteristics of the platform.

After ballast adjustment, all biomimetic platforms maintain the same draft as the original OC4 design, as summarized in Table 5. Due to the additional buoyancy provided by the chambers, extra ballast water is required to satisfy hydrostatic equilibrium, resulting in a moderate increase in total platform mass. Nevertheless, the centers of gravity and moments of inertia remain close to those of the original platform. This ballast adjustment strategy ensures equivalent hydrostatic conditions among all configurations, providing a consistent basis for the subsequent hydrodynamic performance comparison.

4. Numerical modeling and verification

4.1. Computational domain and numerical setting

The computational domain used in this study is a three-dimensional region composed of an upper air layer and a lower water layer, as illustrated in Fig. 7. The overall length of the domain is about sixteen rotor diameters (16D), and the width spans approximately seven rotor diameters (7D). Vertically, the air region extends to a height of 4D above the still water level, while the water depth reaches 3D below it. These dimensions ensure that wave propagation and platform motions can be

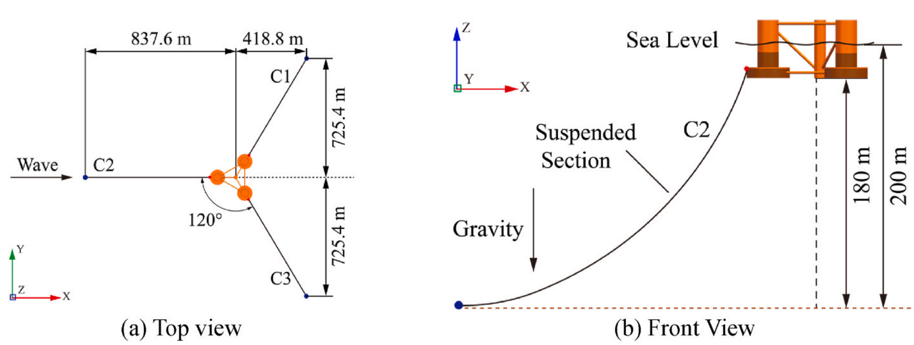

Fig. 5. Schematic diagram of catenary arrangement.

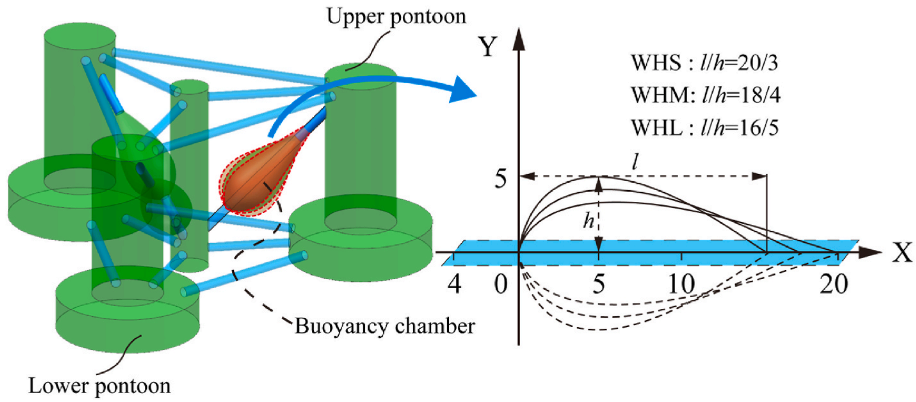

Fig. 6. Water hyacinth-inspired platform and cross-sectional view of the floater.

Table 4
Mass-related parameters of the WH platform (Excluding ballast water).

	Mass/kg	Center of mass/m (below the waterline)	I_{xx}/kg·m^2	I_{yy}/kg·m^2	I_{zz}/kg·m^2
Original	4,662,204.00	−7.42	2.24×10^9	2.24×10^9	3.32×10^9
WHL	4,698,502.50	−7.41	2.24×10^9	2.24×10^9	3.33×10^9
WHM	4,693,156.00	−7.41	2.24×10^9	2.24×10^9	3.33×10^9
WHS	4,689,456.00	−7.41	2.24×10^9	2.24×10^9	3.32×10^9

Table 5
Mass-related parameters of the WH platform (Including ballast water).

	Mass/kg	Center of mass/m (below the waterline)	I_{xx}/kg·m^2	I_{yy}/kg·m^2	I_{zz}/kg·m^2
Original	13,266,384.00	−13.54	6.42×10^9	6.42×10^9	1.11×10^{10}
WHL	14,768,353.00	−13.26	7.06×10^9	7.06×10^9	1.23×10^{10}
WHM	14,149,470.00	−13.42	6.79×10^9	6.79×10^9	1.18×10^{10}
WHS	13,804,916.00	−13.48	6.64×10^9	6.64×10^9	1.15×10^{10}

simulated without significant interference from the domain boundaries. To reduce boundary effects, the floating VAWT is located approximately 300 m downstream of the inlet.

The overset mesh strategy is applied to the platform and rotor regions to allow six-DOF motion of the platform and free rotation of the VAWT. To accurately resolve key flow features such as flow separation, vortex shedding, and free-surface deformation, local mesh refinement is applied near the air-water interface region and in the wake areas behind the rotor and blades. This refinement enhances the ability of the model to resolve complex flow structures. For the three configurations with different buoyancy chamber levels (WHS, WHM, and WHL), separate meshing schemes are established. Additional refinement is applied on the outer surfaces of the buoyancy chambers to ensure sufficient flow resolution near small-scale geometric features. The mesh information for each biomimetic platform and its corresponding floating VAWT system is summarized in Table 6. The mesh size in the WH region gradually decreases from 0.6 m to 0.1 m, and the total number of cells slightly increases with the chamber level.

The turbulence model adopted in this study is the shear stress transport (SST) k-ω model based on the Reynolds-averaged Navier-Stokes equations. This model has been validated in numerical study of floating VAWT and has shown good stability and applicability (Liu et al., 2025). The free surface is tracked using the VOF method to capture the nonlinear characteristics of the air-water interface. At the inlet boundary, a fifth-order Stokes regular wave with a height of 7.58 m and a period of 12.1 s is applied. The wave parameters are derived from measured ocean-wave data in the South Atlantic Ocean (50.96°S, 13.31°W), a region characterized by persistent swell activity and energetic sea states. Such conditions are representative of a harsh offshore environment and are therefore suitable for evaluating the stabilization capability of the proposed biomimetic platforms under severe wave loading. A damping zone of 600 m is set at the outlet to eliminate wave reflections and ensure numerical convergence.

4.2. Turbulence model validation

To verify the accuracy of the adopted CFD methodology, a validation study was conducted using the wind tunnel experiments of Battisti et al. (2018), which provide detailed measurements of the aerodynamic performance and wake characteristics of an H-type VAWT. The numerical model was established according to the reported geometric parameters and operating conditions, and the SST k-ω turbulence model was employed for the simulations.

Fig. 8 compares the predicted power coefficient C_P with the experimental measurements at different tip speed ratios (TSRs). The numerical results agree well with the experimental data and successfully reproduce the variation trend of C_P over the entire operating range. The predicted optimum TSR and peak power coefficient are also captured with good accuracy, indicating that the adopted turbulence model can reliably predict the aerodynamic performance of the VAWT.

Further validation was performed through comparisons of the wake velocity and turbulence intensity distributions at downstream locations of 0.75D and 1.5D, as shown in Fig. 9. The CFD results show good agreement with the experimental measurements under different inflow velocities, accurately capturing both the velocity deficit and wake recovery characteristics. In addition, the predicted turbulence intensity distributions reasonably reproduce the locations and magnitudes of the experimental peaks.

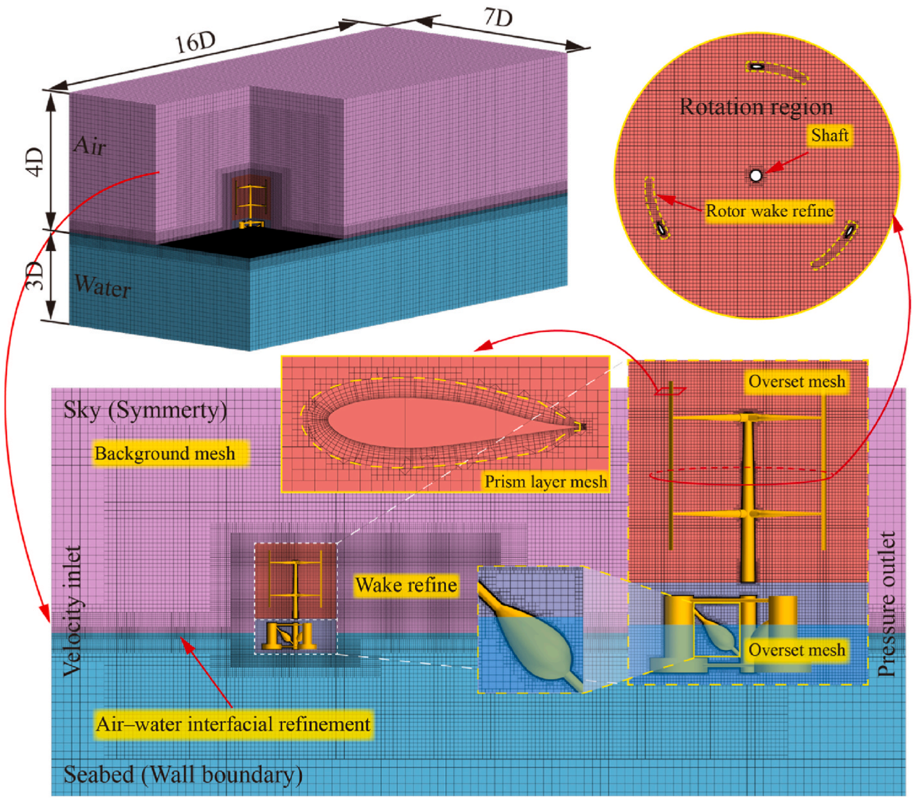

Fig. 7. Mesh distribution of the floating VAWT with different WH buoyancy chamber levels.

Table 6
Grid number for the individual platform and floating VAWT.

Parameter	Original	WHS	WHM	WHL
Grid size in WH region	0.6	0.4	0.2	0.1
Grid number of the individual platform	7883350	7961640	7980858	8004394
Grid number of floating VAWT	13901460	13980178	13998361	14022932

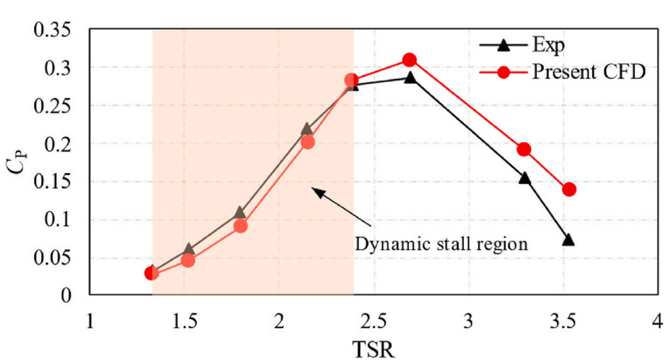

Fig. 8. Comparison of C_P results under different TSRs.

Overall, the comparisons demonstrate that the present CFD framework provides satisfactory predictions of both aerodynamic performance and wake evolution, thereby establishing confidence in its application to the subsequent numerical simulations.

4.3. Hydrodynamic validation

To verify the accuracy of the hydrodynamic modelling approach, a free-decay test of the OC4 semi-submersible platform was conducted and compared with published numerical results. As shown in Fig. 10, the turbine and tower were represented by an equivalent concentrated mass, and the platform was released from prescribed initial offsets in the pitch and surge directions. The initial pitch angle was 8 deg, while the initial surge displacement was 22 m. The present CFD DFBI results were compared with the DFBI results reported in Tran et al. (Tran and Kim, 2016) and the naoeFoam results reported in Cheng et al. (2019).

Fig. 11 shows the comparison of pitch and surge free-decay responses. For the pitch motion, the present results agree well with the two reference solutions in both natural period and decay trend, indicating that the restoring moment and hydrodynamic damping are well captured. For the surge motion, the present results also reproduce the main oscillation period and amplitude attenuation, although small phase differences appear in the later stage of the decay. These differences may be caused by different treatments of viscous damping, free-surface modelling, and mooring restoring forces among the CFD solvers. Overall, the agreement confirms that the present DFBI-based numerical framework can reasonably predict the hydrodynamic restoring and damping characteristics of the floating platform, supporting its use in the following hydrodynamic response analysis.

4.4. Grid and time-step sensitivity analysis

The computational domain was discretized using the Trim Mesher in STAR-CCM+, with prism layers applied near solid surfaces to accurately resolve the boundary-layer flow. A total of 8 prism layers were generated, with a first-layer thickness of 5×10^{-3} m and a total prism-layer thickness of 0.28 m. The all-y^+ wall treatment was adopted in combination with the SST k-ω turbulence model, resulting in wall y^+ values mainly within the range of 50-150, which satisfies the recommended

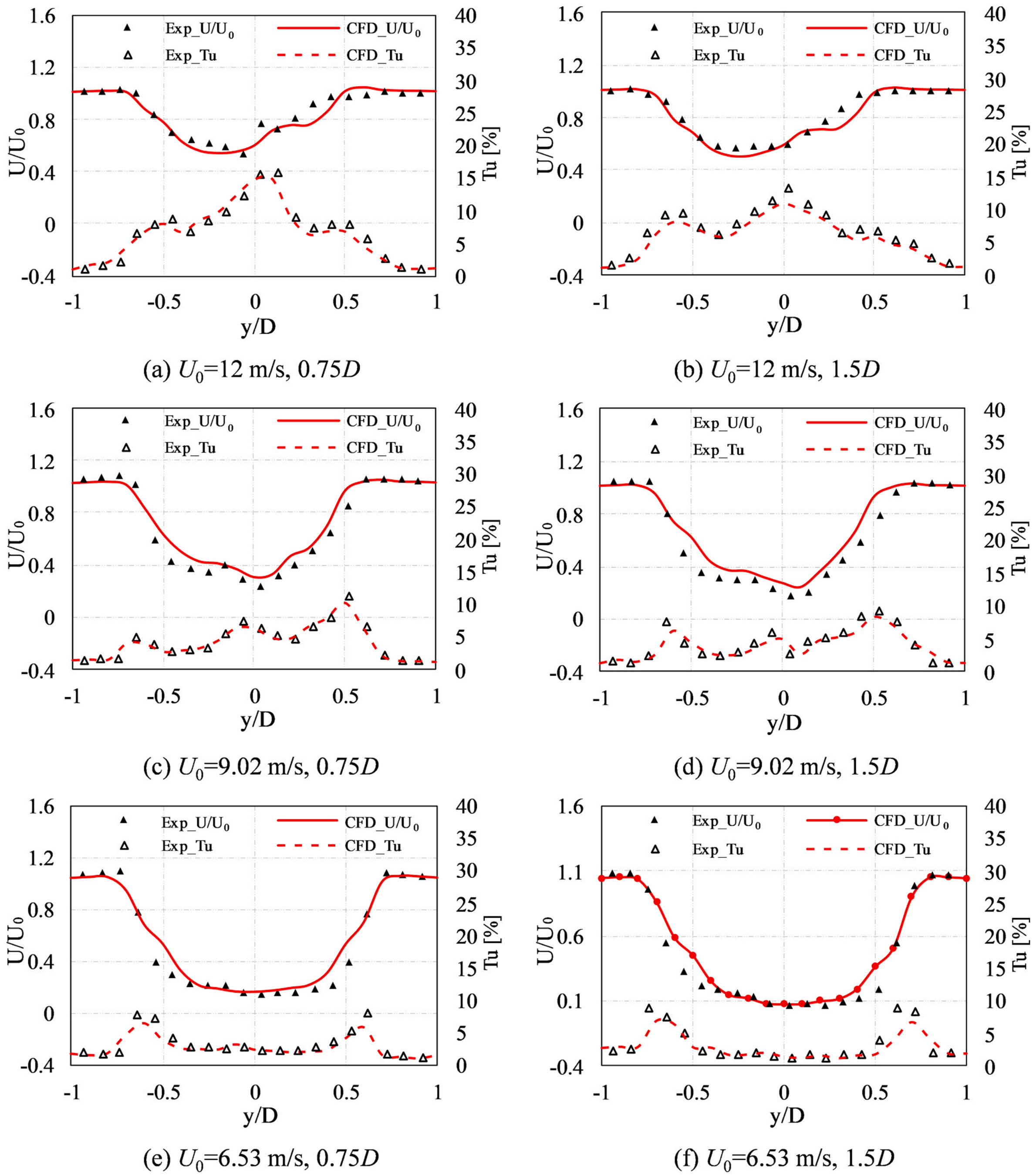

Fig. 9. Comparison of downstream velocity distributions at different TSRs.

requirements for wall-function-based simulations. It should be noted that the present study employs a full-scale floating VAWT model. Resolving the boundary layer with ($y^+ \approx 1$) would lead to a prohibitive increase in the overall mesh count and computational cost. Therefore, the all-y^+ wall treatment was considered a reasonable compromise between numerical accuracy and computational efficiency. Three mesh schemes were generated for the original floating VAWT, including a coarse mesh (10.46 million cells), a medium mesh (13.90 million cells), and a fine mesh (16.97 million cells), as summarized in Table 7. The mesh refinement was mainly concentrated in the rotor wake, overset region, blade surface, and blade wake.

As shown in Table 7, the average skewness angle gradually decreases from 9.43° to 7.90°, while the average orthogonal quality increases from 0.9286 to 0.9424 with mesh refinement, indicating consistently high mesh quality for all three schemes. To evaluate mesh convergence, the instantaneous torque coefficient (C_M) of a blade over one complete revolution was selected as the assessment parameter. The corresponding results are presented in Fig. 12a. It can be observed that the coarse, medium, and fine mesh solutions exhibit very similar distributions over the entire azimuthal cycle. The largest differences occur near the primary peak around 90° and the secondary peak around 240°. However, the medium and fine mesh curves almost overlap, indicating that further refinement has a negligible influence on the predicted aerodynamic loads. Considering both numerical accuracy and computational cost, the medium mesh was adopted for the subsequent simulations.

A time-step sensitivity analysis was subsequently performed using the medium mesh. Six time-steps, namely 0.05 s, 0.04 s, 0.03 s, 0.02 s, 0.01 s, and 0.005 s, were examined under identical operating conditions.

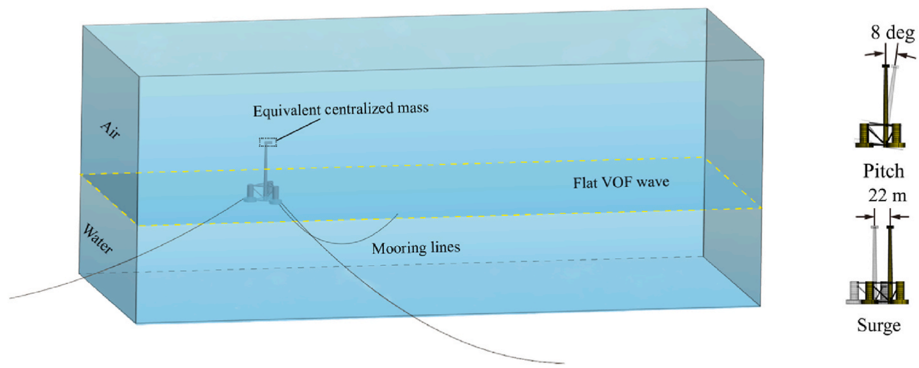

Fig. 10. Schematic diagram of free decay test for OC4 platform.

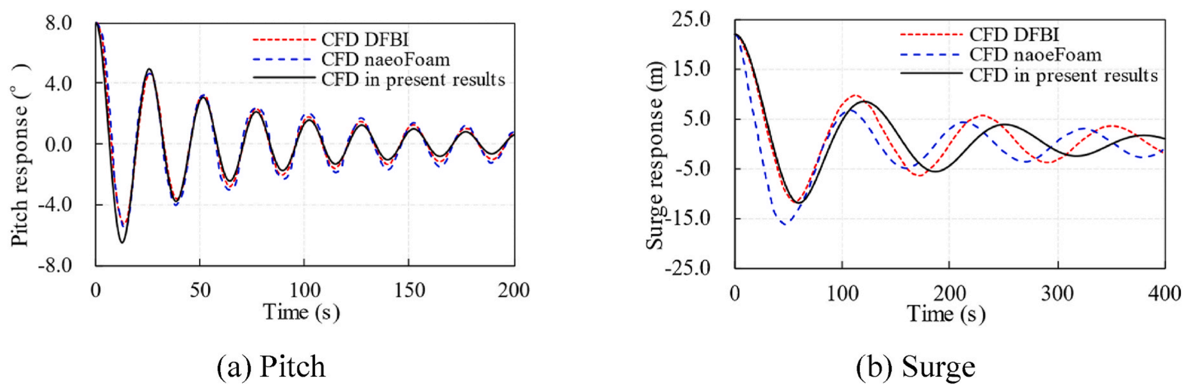

Fig. 11. Comparison of free decay numerical experiment result of FOWT.

Table 7
Grid sensitivity analysis for floating VAWTs.

Parameters	Coarse mesh	Medium mesh	Fine mesh
Rotor wake size [m]	2.5 m	1.25 m	1.25 m
Overset region size [m]	2.5 m	1.25 m	0.625 m
Blade surface size [m]	0.3125 m	0.15625 m	0.078125 m
Blade wake size [m]	0.625	0.3125 m	0.3125 m
Total cell count	10462219	13901460	16969013
Skewness angle (avg.)	9.4325	8.4401	7.8963
Orthogonal quality (avg.)	0.9286	0.9316	0.9424

Fig. 12b compares the corresponding instantaneous torque coefficient distributions. The results show that the largest differences occur near the first torque peak around an azimuth angle of 90°. As the time step decreases, the torque curves gradually converge. Noticeable deviations are observed for the larger time steps of 0.05 s and 0.04 s, whereas the results obtained using 0.02 s, 0.01 s, and 0.005 s are very close throughout the entire rotation cycle. In particular, the curves corresponding to 0.01 s and 0.005 s almost completely overlap, indicating that the temporal discretization error has become negligible. Considering both numerical accuracy and computational cost, a time step of 0.01 s was adopted for all subsequent simulations.

5. Results and discussion

5.1. Hydrodynamic response of biomimetic platform configurations

This section investigates the hydrodynamic behavior of the original platform and the three WH configurations, including the six-DOF motions, the tension responses of the catenary mooring system, and the flow field characteristics around the platforms. Please note that the ballast water in all platforms was adjusted to maintain a draft comparable to that of the NREL OC4 semi-submersible design to ensure a consistent comparison.

5.1.1. Six-DOF motion

The time-domain responses of three translational motions (surge, sway, and heave) and the three rotational motions (roll, pitch, and yaw) are shown in Fig. 13. These results are used to assess how the buoyancy chamber geometry influences the global hydrodynamic performance of the platform.

As shown in Fig. 13, the biomimetic platforms exhibit different response characteristics compared with the original platform. The most significant variations appear in surge, heave, and pitch, which display clear periodic oscillations under regular wave excitation and dominate the overall platform motion. This behavior arises from the combined effects of wave-induced horizontal inertia forces, buoyancy variations, and pitching moments. In contrast, sway, roll, and yaw remain relatively small due to the symmetric platform layout and weaker excitation, and therefore represent secondary response modes. For the surge response (Fig. 13a), all platforms show pronounced periodic oscillations. Compared with the original platform, the biomimetic configurations show increasing surge responses as the buoyancy chamber size increases. In particular, the WHL platform exhibits the largest displacement and a noticeable growth in peak values after (t = 240) s. This trend

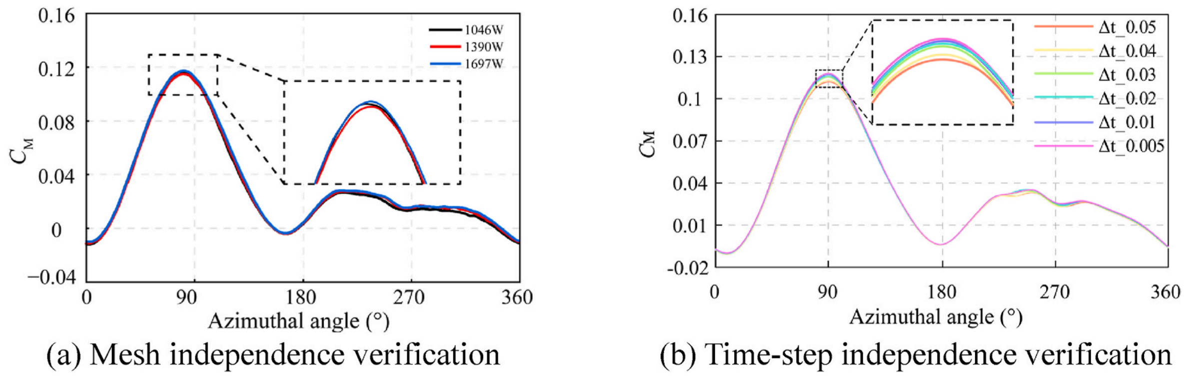

Fig. 12. Mesh and time-step independence verification based on instantaneous torque coefficient.

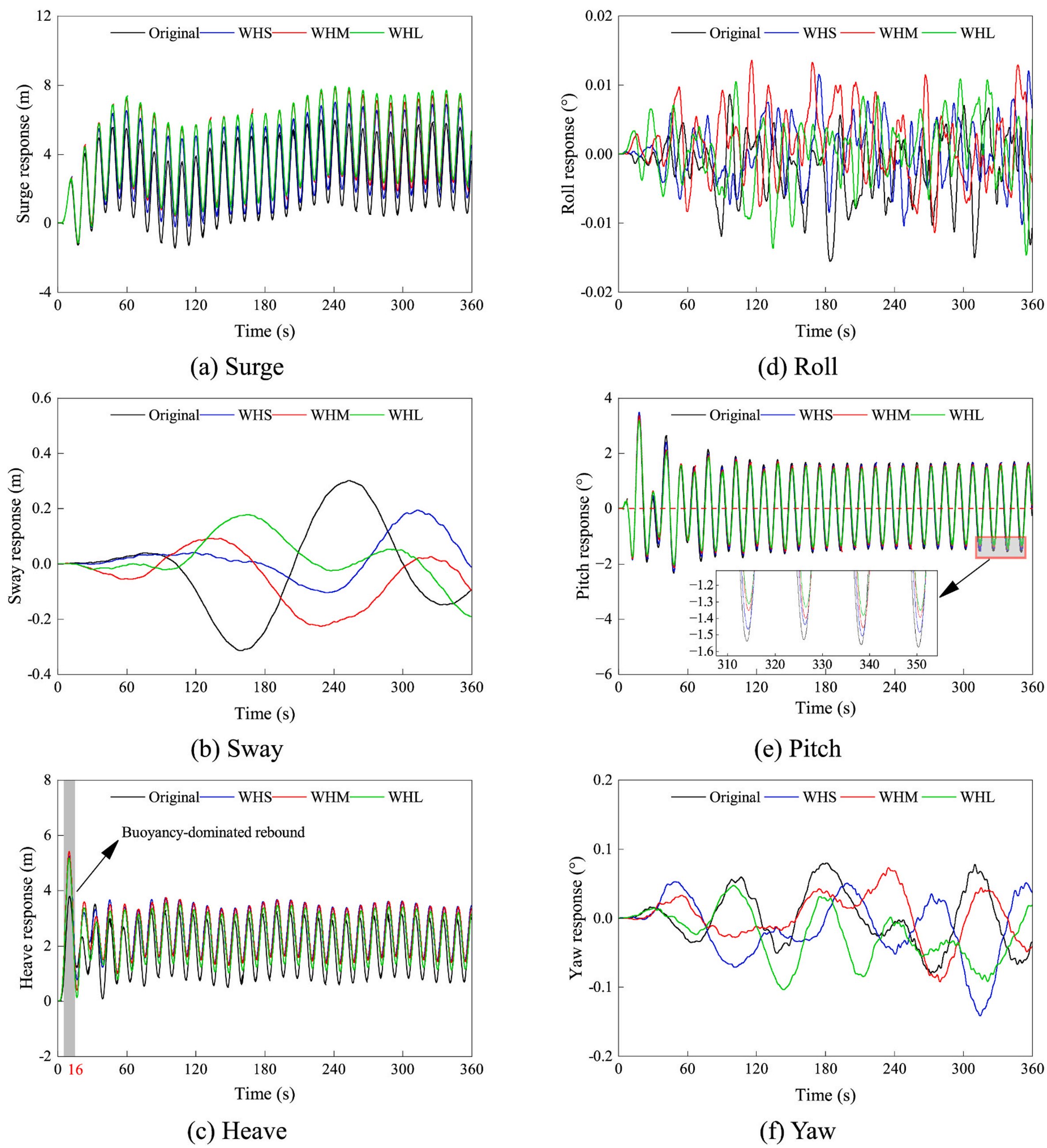

Fig. 13. Six-DOF response of the floating platforms with and without buoyancy chamber.

is mainly attributed to the larger wave-facing area and increased local added mass introduced by the large buoyancy chambers, which enhance the wave-induced drift along the wave propagation direction.

A similar periodic behavior is observed in the heave response (Fig. 13c). During the initial stage, the biomimetic platforms experience a short buoyancy-dominated rebound because they are released from the same initial position as the original platform. After reaching a stable oscillation state, the biomimetic platforms exhibit higher upward displacements near wave crests but smaller overall heave amplitudes than the original platform, particularly for the WHM and WHS cases. This indicates that the buoyancy chambers not only increase the instantaneous buoyancy but also enhance the vertical restoring stiffness and hydrodynamic damping, thereby suppressing downward motion near the wave troughs. The pitch response shown in Fig. 13e gradually converges to a stable oscillation pattern after the initial transient stage. All biomimetic platforms exhibit slightly smaller pitch amplitudes than the original platform, with the WHS configuration providing the greatest reduction. This demonstrates the beneficial effect of the buoyancy chambers on pitch stability. By comparison, the sway (Fig. 13b), roll (Fig. 13d), and yaw (Fig. 13f) responses remain relatively small throughout the simulation. The original platform exhibits a noticeable drift in the sway direction, whereas the biomimetic platforms effectively suppress this motion through enhanced lateral hydrodynamic restoring effects. Roll and yaw amplitudes remain below 0.5°, indicating a negligible influence on the overall platform dynamics.

To further quantify the response characteristics of biomimetic platforms, The statistical values of the dominant surge, heave, and pitch motions are summarized in Table 8.

For the surge response, the WHS platform exhibits the best suppression performance. Compared with the original platform, its fluctuation amplitude decreases from 4.97 m to 4.16 m, while the standard deviation decreases from 1.82 m to 1.27 m, corresponding to reductions of 16.3% and 30.2%, respectively. In contrast, the WHL platform shows the largest surge response, with an amplitude of 5.10 m and a standard deviation of 1.98 m. The WHM platform lies between these two cases and maintains a relatively moderate surge motion. In the heave direction, all biomimetic platforms exhibit smaller amplitudes and standard deviations than the original platform. The heave amplitudes of the WHL, WHM, and WHS platforms decrease by 10.3%, 15.5%, and 15.5%, respectively. Among them, the WHM platform achieves the lowest standard deviation of 0.60 m, representing a reduction of 25.0% compared with the original platform, indicating the most stable vertical response. A similar trend is observed for the pitch motion. The pitch amplitudes of the WHL, WHM, and WHS platforms are reduced by 13.8%, 12.3%, and 15.0%, respectively. The WHS platform exhibits the lowest standard deviation of 0.83°, corresponding to a reduction of 30.3%, while the WHL and WHM platforms also provide consistent pitch suppression relative to the original platform.

Overall, the three biomimetic configurations improve platform stability to different extents. WHS provides the strongest suppression of surge and pitch motions, whereas WHL exhibits the largest surge response despite its improved heave and pitch performance. The WHM platform maintains relatively low amplitudes and standard deviations in all three dominant degrees of freedom, particularly in the heave direction. Considering the combined performance in surge, heave, and pitch, the WHM configuration provides the most balanced dynamic behavior and is therefore selected as the optimal biomimetic design for subsequent analyses.

Table 8
Statistical values of surge, heave, and pitch responses for the original and WH platforms.

	Statistical values	Original	WHL	WHM	WHS
Surge/m	Maximum value	5.77	7.86	7.40	6.94
	Minimum value	0.80	2.76	2.46	2.78
	Fluctuation amplitude	4.97	5.10	4.95	4.16
	Standard deviation	1.82	1.98	1.88	1.27
Heave/m	Maximum value	2.95	3.15	3.45	3.37
	Minimum value	0.64	1.08	1.49	1.41
	Fluctuation amplitude	2.32	2.08	1.96	1.96
	Standard deviation	0.80	0.70	0.60	0.66
Pitch/°	Maximum value	1.70	1.50	1.53	1.29
	Minimum value	−1.56	−1.31	−1.33	−1.47
	Fluctuation amplitude	3.26	2.81	2.86	2.77
	Standard deviation	1.19	1.07	1.12	0.83

5.1.2. Mooring lines tension

Fig. 14 shows the time-domain tension responses of the three mooring lines, C1, C2, and C3, during the steady-state stage. Overall, the three biomimetic platforms lead to a redistribution of tension within the mooring system. The C2 line, which is aligned with the incident wave direction, is highly sensitive to the surge motion of the platform, while C1 and C3 on the two sides mainly experience additional fluctuations caused by sway and rotational motions.

From the tension response curves of C2, it can be observed that the peak tensions of all WH biomimetic platforms are higher than that of the original platform. As the buoyancy chamber level increases, meaning thicker chambers and a shorter longitudinal projection length, the peak tension rises further, following the order WHL > WHM > WHS. This indicates that the buoyancy chambers enlarge the wave-facing area of the platform, amplify the surge displacement and produce a greater forward motion of the platform's front section. As a result, the C2 line experiences higher stretching and increased tension. In contrast, the tensions of C1 and C3 gradually decrease with increasing buoyancy chamber level, and their peak values follow the order Original > WHS > WHM > WHL, which is opposite to the trend observed for C2. This is because when the platform is pushed forward by the wave, the lateral mooring lines (C1 and C3) become partially slackened, leading to a reduction in tension.

This phenomenon is highly consistent with the six-DOF response results presented in Section 5.1, where the increase of surge motion is most prominent for the biomimetic platforms. The additional mass effect created by the buoyancy chambers and their influence of the platform's inertial response intensify the dynamic motion in the wave-facing direction, directly increasing the tension in C2. In contrast, the sway and yaw motions remain relatively small, producing limited lateral excitation on C1 and C3, and causing a more noticeable reduction in their tension.

A more detailed engineering evaluation of this response pattern is provided by examining its influence on the load distribution and structural safety of the mooring system, Table 9 summarizes the maximum, minimum, and mean tensions of the three catenary lines under different platform configurations, together with their corresponding safety factors. Such data provides a more quantitative and practical basis for evaluation.

As shown in Table 9, the introduction of the biomimetic buoyancy chambers improves the safety factors of the lateral mooring lines C1 and C3. The WHL platform achieves the highest values of 6.61 for line C3, indicating that the biomimetic structures help reduce lateral motion and side mooring loads, thereby enhancing the overall safety of the system. In contrast, the main mooring line C2 in the wave facing direction shows the opposite trend. In the WH platforms, the maximum tension of C2 increases significantly, leading to a slight decrease in its safety factor. The safety factor of C2 decreases from 5.66 in the original platform to 5.30, 5.34, and 5.44 for the WHL, WHM, and WHS platforms, respectively. This suggests that while the biomimetic structures improve resistance to incident waves, they also concentrate the tensile load on the main mooring line C2.

According to the API-RP-2SK standard (American Petroleum Institute, 2001), when a mooring system is intact and designed using a quasi-static approach, the maximum allowable tension in a catenary line should not exceed 50% of its breaking strength, corresponding to an equivalent safety factor of 2.0. In the present simulations, the safety

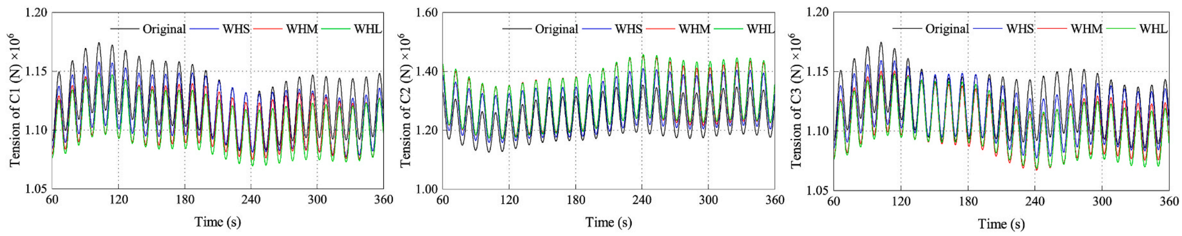

Fig. 14. Time-history comparison of mooring line tensions for the original and WH platforms.

Table 9
Safety factor analysis of mooring system.

	Catenary No.	Maximum	Minimum	Average	Safety Factor
Original	C1	1157999	1097329	1124242	6.48
	C2	1325154	1159682	1239053	5.66
	C3	1151015	1092633	1118337	6.52
WHL	C1	1129412	1074499	1099518	6.64
	C2	1415152	1206788	1310205	5.30
	C3	1134558	1082549	1104419	6.61
WHM	C1	1131552	1081208	1102824	6.63
	C2	1404970	1206040	1305426	5.34
	C3	1137667	1081512	1106960	6.60
WHS	C1	1141663	1085206	1110434	6.57
	C2	1379127	1187580	1280403	5.44
	C3	1145833	1088824	1114254	6.55

factors of all three catenary lines in every platform configuration are well above this lower limit, with the minimum value still reaching 5.30. This indicates that the biomimetic buoyancy chamber structures regulate the platform's dynamic responses and mooring load distribution without compromising overall safety. Furthermore, the mooring systems of the WH platforms retain substantial safety redundancy, which is sufficient to ensure long-term operational stability under moderate sea conditions.

5.1.3. *Flow field of the biomimetic platform*

To further clarify the physical mechanisms through which the biomimetic buoyancy chambers regulate the dynamic response of the platform, Fig. 15 presents the instantaneous streamlines, represented by the Y-direction vorticity, together with the pressure distributions of the original platform and the three WH biomimetic platforms during surge motion along the X-axis. Fig. 15a corresponds to the platform moving in the negative X-direction, that is, against the incoming waves, while Fig. 15b shows the motion in the positive X-direction, following the wave propagation. The comparison shows that the buoyancy chambers noticeably influence the flow-field patterns, local pressure distribution, and that the extent of these effects varies with the chamber level.

During platform motion in the negative X-direction (wave-facing stage, Fig. 15a, left column), the cylindrical braces of the original platform are directly exposed to the incoming flow and generate strong flow acceleration and a pronounced separation–stagnation region. The streamline patterns show a clear high-vorticity band forming downstream of the braces, characterized by unsteady separation and periodic vortex roll-up. These vortical structures stretch downstream and interact with the main columns, producing significant local dynamic-pressure variations and strong transient hydrodynamic loading. In comparison, all three WH configurations produce a smoother transition zone because the buoyancy chambers introduce a curved guiding surface upstream of the braces. These pre-conditions and redirects the incident flow before it reaches the brace region, delaying flow separation and improving flow attachment. As a result, the pressure gradient on the wave-facing side becomes smoother, the separated vortices become smaller and less coherent, and the overall flow field exhibits reduced unsteadiness with enhanced viscous-damping characteristics. The instantaneous surge velocities further confirm these trends. The original platform reaches −1.15 m/s, whereas WHS (−1.09 m/s), WHM (−1.06 m/s), and WHL (−1.03 m/s) all show reduced magnitudes. This reduction reflects the increased added mass and hydrodynamic damping induced by the biomimetic chambers, which effectively suppress the platform's acceleration and velocity response in the wave-facing direction.

In the wave-following phase (Fig. 15b, right column), the relative backward motion with respect to the propagating waves produces a large low-velocity recirculation region behind the braces. In the original configuration, a compact cluster of high-vorticity structures forms downstream of the brace due to shear-layer roll-up. By contrast, the WH platforms show elongated vorticity filaments above the brace, generated by the shielding and guiding effect of the buoyancy chambers. These stretched vortical bands indicate stronger flow deflection and extended shear-layer development. The instantaneous surge velocities also exhibit modest reductions. The original platform reaches 1.18 m/s, while the WHS, WHM, and WHL platforms reach 1.16 m/s, 1.15 m/s, and 1.12 m/s, respectively. This pattern aligns with the enhanced viscous dissipation and directional damping generated by the buoyancy chambers during the wave-following stage.

Overall, the biomimetic buoyancy chambers fundamentally alter the local flow topology in both wave-facing and wave-following conditions. They delay separation, weaken shear-layer instabilities, and suppress strong unsteady vortex dynamics, thereby reducing instantaneous platform velocities and hydrodynamic pulsation levels. Among the three configurations, WHL shows the strongest interference effect due to its larger chamber volume, while WHS still improves flow attachment despite its smaller size. WHM achieves the most balanced control between damping enhancement and flow disturbance, making it the most promising configuration for engineering application.

5.2. *Comparison with conventional buoyancy structures*

To further evaluate the influence of buoyancy geometry on platform stability, three conventional buoyancy structures, namely cylinder, disc, and sphere, were introduced for comparison with the WHM configuration. All auxiliary buoyancy bodies were designed with the same volume as the WHM chamber, and the ballast water was adjusted to ensure identical draft depths. The corresponding geometric dimensions and mass properties are provided in Appendix A. Since Section 5.1 has shown that surge, heave, and pitch are the dominant response modes of the platform, only these three degrees of freedom are compared in this section.

5.2.1. *Comparison of dominant motion responses*

Fig. 16 presents the motion responses over two wave periods. For the heave response (Fig. 16a), the four platforms exhibit similar oscillation amplitudes and mean positions, with average values close to 2.45 m. However, the sphere configuration shows a noticeable phase delay and the largest heave amplitude. This behavior is likely related to the smaller spatial occupation of the spherical buoyancy body along the brace, causing the wave excitation to reach the supporting structure later and resulting in a delayed vertical response.

For the pitch response (Fig. 16b), the differences among the four configurations are relatively small. Nevertheless, the WHM platform

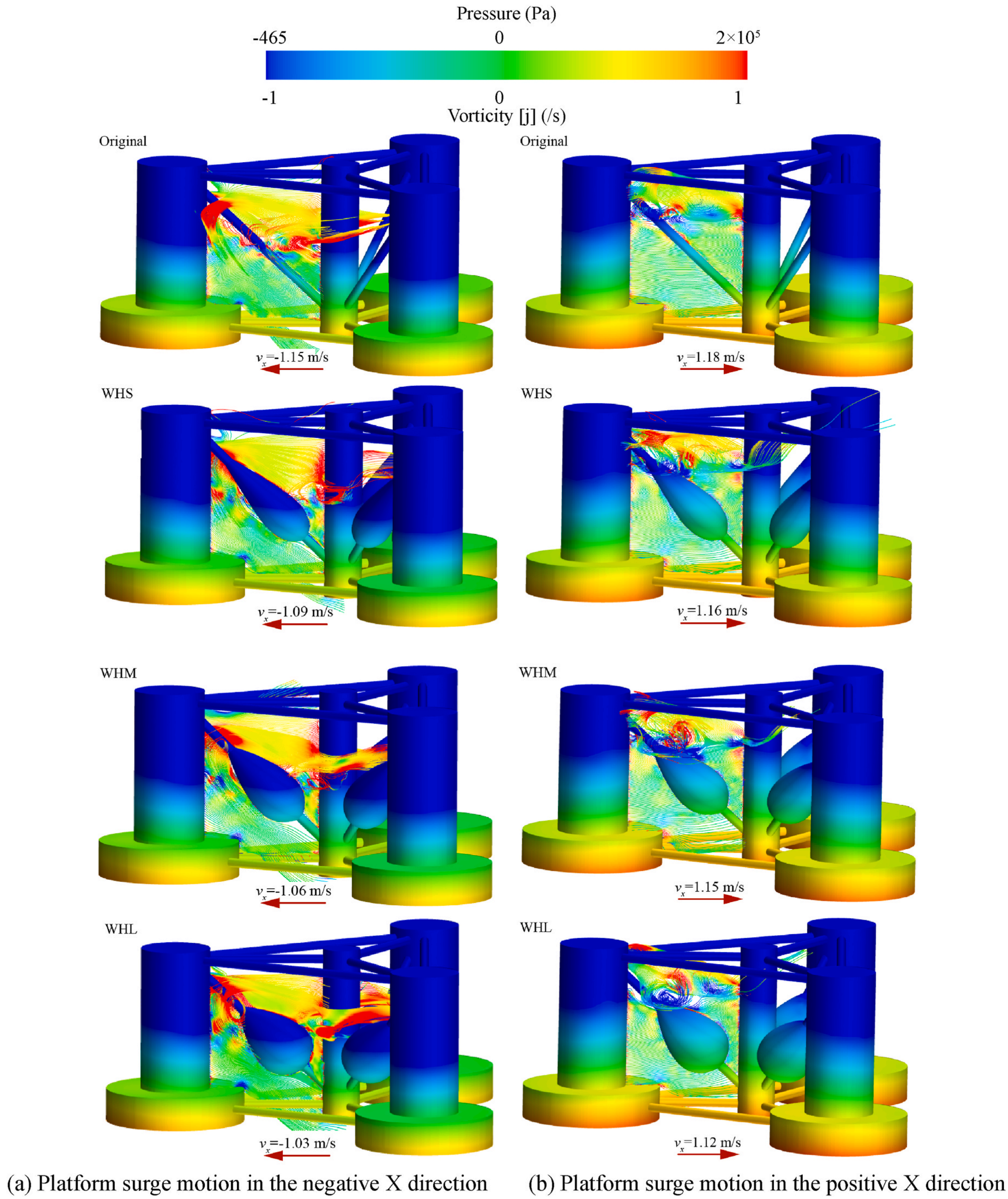

Fig. 15. Flow streamlines and pressure contours of the original and WH platforms.

consistently exhibits slightly lower peak values and fluctuation amplitudes than the conventional geometries, indicating a moderate reduction in rotational response around the transverse axis. The largest differences are observed in the surge response (Fig. 16c). The sphere and disc configurations reach maximum surge displacements of approximately 7.20 m and 6.65 m, respectively, which are significantly larger than those of the cylinder (6.17 m) and WHM platform (6.19 m). This trend can be attributed to the larger projected areas of the sphere and disc in the wave propagation direction, which increase the wave-induced excitation force acting on the platform. Consequently, greater drift is generated under wave loading. In comparison, the cylinder and WHM configurations exhibit relatively smaller surge responses, indicating a reduced sensitivity to wave-induced horizontal loading.

5.2.2. Comparison of flow mechanisms

To further explain the response differences observed in Figs. 16 and 17 compares the instantaneous vorticity distributions around the four buoyancy configurations. The left column corresponds to the stage when the platform moves against the wave direction, whereas the right column represents the stage when the platform moves in the same direction as the propagating wave.

When the platform moves against the wave direction, the relative flow directly impacts the auxiliary buoyancy structures. For the WHM, disc, and sphere configurations, the curved surfaces guide the incoming

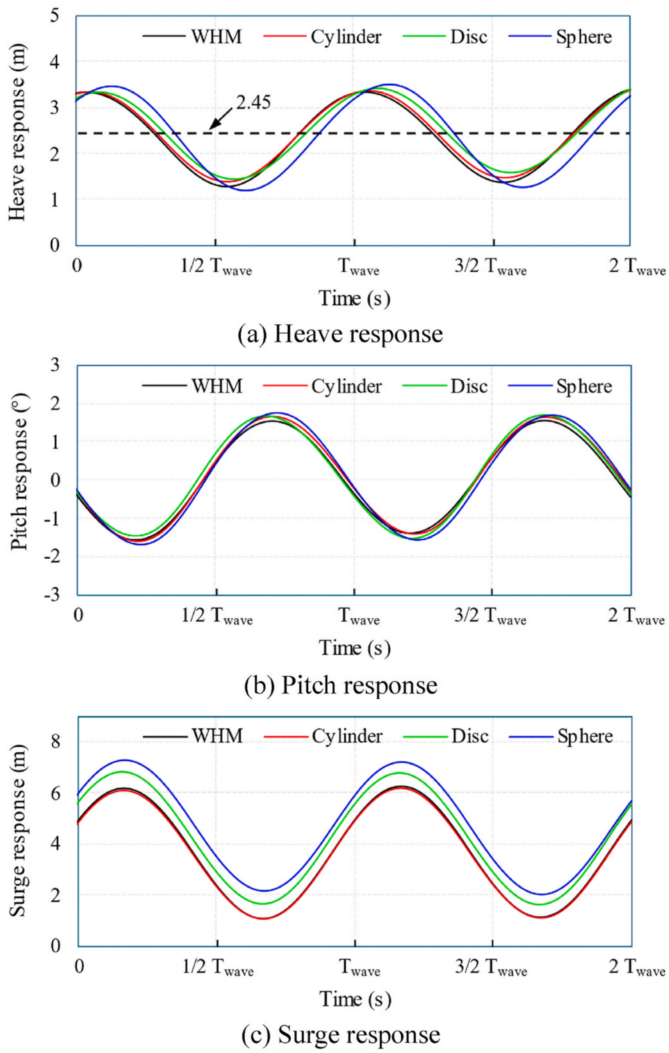

Fig. 16. Comparison of dominant motion responses between the WHM platform and conventional buoyancy structures of equivalent volume.

flow more smoothly, and the flow separation regions remain relatively limited. By contrast, the cylinder exhibits a more obvious separated vortex region due to its geometric discontinuity and sharp transition at the edge. This indicates that the cylindrical geometry is more likely to produce local flow separation and unsteady pressure fluctuations under wave impact. Although the instantaneous velocities of the four platforms in this phase are close, the stronger local impact and vortex shedding around the cylinder may increase structural vibration and fatigue risk in long-term operation. When the platform moves in the same direction as the wave, the wave particle velocity remains higher than the platform velocity, leading to local reverse flow and recirculation around the buoyancy structures. In this stage, the three conventional configurations show slightly larger platform velocities than WHM, indicating that their larger hydrodynamic resistance and wave-facing load transfer more wave energy into platform motion. This agrees with the motion response results in Fig. 16, where the sphere and disc produce larger surge responses. In contrast, the WHM configuration shows a lower surge velocity, suggesting that its streamlined geometry weakens direct wave loading and reduces the conversion of wave force into platform translation.

Overall, the motion and flow-field results indicate that the hydrodynamic performance of the auxiliary buoyancy structures is strongly influenced by both wave-load transfer and flow separation characteristics. The sphere and disc configurations generate larger surge responses because of their greater projected areas in the wave direction, while the cylinder exhibits more pronounced flow separation and vortex shedding due to its geometric discontinuity. In contrast, the WHM configuration combines relatively low surge, heave, and pitch responses with a smoother flow pattern around the braces. This suggests that the biomimetic profile can effectively balance wave-force reduction and flow stability. Therefore, among the investigated configurations, the WHM platform exhibits the most favorable overall hydrodynamic performance and is selected for the subsequent floating VAWT analysis.

5.3. Aerodynamic-hydrodynamic responses of biomimetic floating VAWT

The previous section concludes that the WHM platform offers the best overall stability among the three biomimetic configurations. Based on this result, the WHM structure is incorporated into a full floating VAWT system in this section. The aerodynamic performance, hydrodynamic response, and their coupled behavior are examined to further evaluate its engineering applicability.

5.3.1. Power coefficient and flow field

The power coefficients of the floating VAWT with and without the WHM structure are compared to assessing the effect of the buoyancy chamber, as shown in Fig. 18.

In the initial stage, the fluctuations remain mild because the incident waves have not yet reached the platform and the relative inflow experienced by the rotor changes only slightly. As the waves arrive, both curves enter a periodic state. The mean power coefficient calculated over the final ten steady revolutions is 0.336 for the WHM configuration and 0.341 for the configuration without WHM, a difference of only about 1.5%, which is negligible. However, the standard deviation for the WHM case decreases by about 8%, indicating a clear reduction in power fluctuations. These results indicate that the biomimetic buoyancy chambers help smooth the power fluctuation of the floating VAWT while maintaining a comparable wind energy extraction capability.

A Fourier transform is employed to analysis the frequency characteristics of the power coefficient. Fig. 19 presents the power spectral density (PSD), which identifies the dominant frequency components of the power fluctuations.

In Fig. 19, the PSD curves reveal a prominent peak around 1.02 Hz, corresponding to the 9P harmonic of the rotor rotation. Both the original and WHM floating VAWT exhibit similar fundamental frequency characteristics, indicating comparable periodic dynamics. However, the WHM configuration demonstrates an 18.6% reduction in PSD amplitude at this dominant frequency and a notably smoother high-frequency response. This indicates that the biomimetic buoyancy chambers design effectively mitigates both low-frequency and high-frequency fluctuations, leading to a more stable and less volatile power coefficient response.

To better understand the physical mechanisms behind the smoother power output of the floating VAWT with the biomimetic chambers, the platform motions that drive the unsteady inflow must first be examined. Fig. 20 shows the time histories of surge, heave, and pitch over one complete wave cycle. Four characteristic instants, corresponding to 1/4 T_{wave}, 1/2 T_{wave}, 3/4 T_{wave}, and T_{wave}, are marked on these curves. These points indicate whether the platform is moving against or along the incoming waves, whether the pitch angle is approaching its maximum or returning toward its neutral position, and whether the heave displacement is rising or falling. They provide the phase reference for interpreting the flow fields.

Using these four instants as the sampling phases, Fig. 21 presents the instantaneous flow field contours and local vorticity structures around the floating VAWT, comparing the configurations with and without the WHM structures. The visualization combines velocity magnitude contours, Q-criterion iso-surfaces ($Q = 0.15\ s^{-2}$), and streamlines to capture both large-scale wake features and small-scale vortex dynamics.

In Fig. 21, a clear velocity-deficit region can be seen behind the rotor

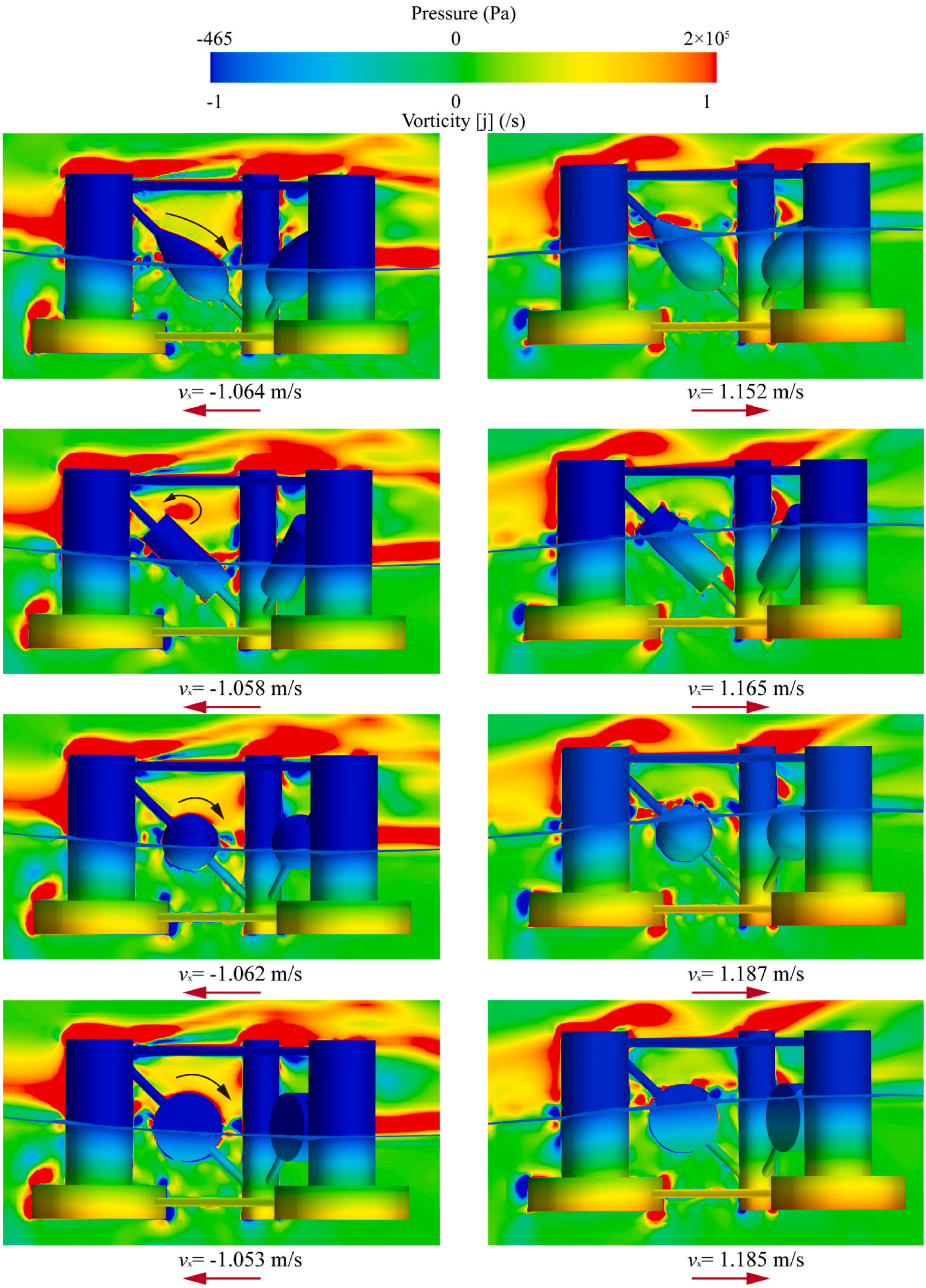

Fig. 17. Vorticity distributions around the WHM and conventional buoyancy structures under opposite and following wave motions.

over a complete wave cycle. At different phase instants, the wake patterns of the floating VAWT with and without the WHM structure appear largely similar, and only minor differences can be identified in the far wake. More evident distinctions emerge when examining the local vorticity fields near the platform braces.

At 1/4 T_{wave} (Fig. 21a and b), the pitch angle of the original platform increases as it moves against the incoming waves. Distinct alternating vortex shedding develops around the cylindrical braces, forming a

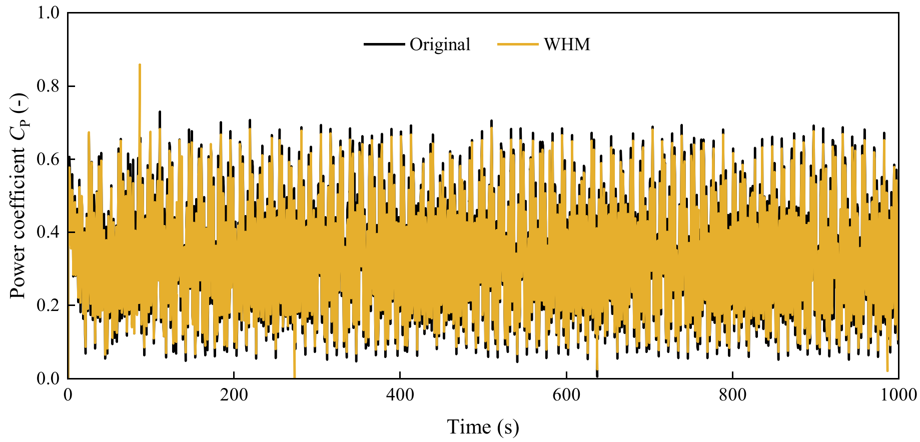

Fig. 18. Comparison of power coefficients for floating VAWT with and without WH configuration.

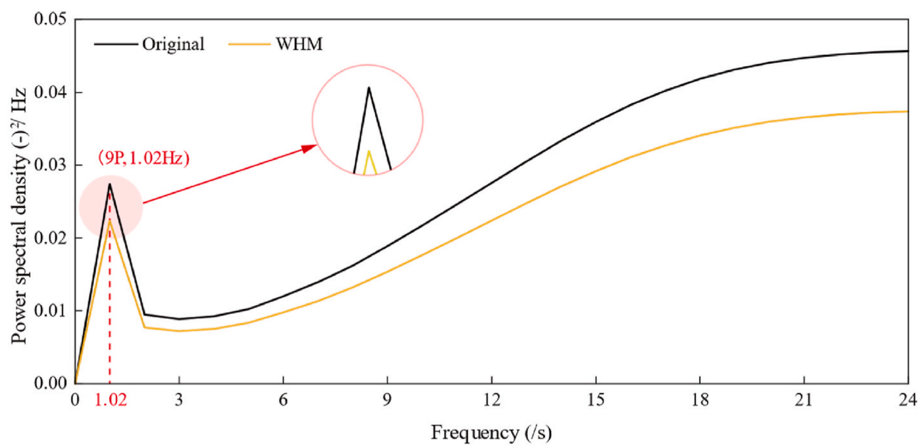

Fig. 19. Power spectral density of the power coefficient for the floating VAWT with and without the WHM structure.

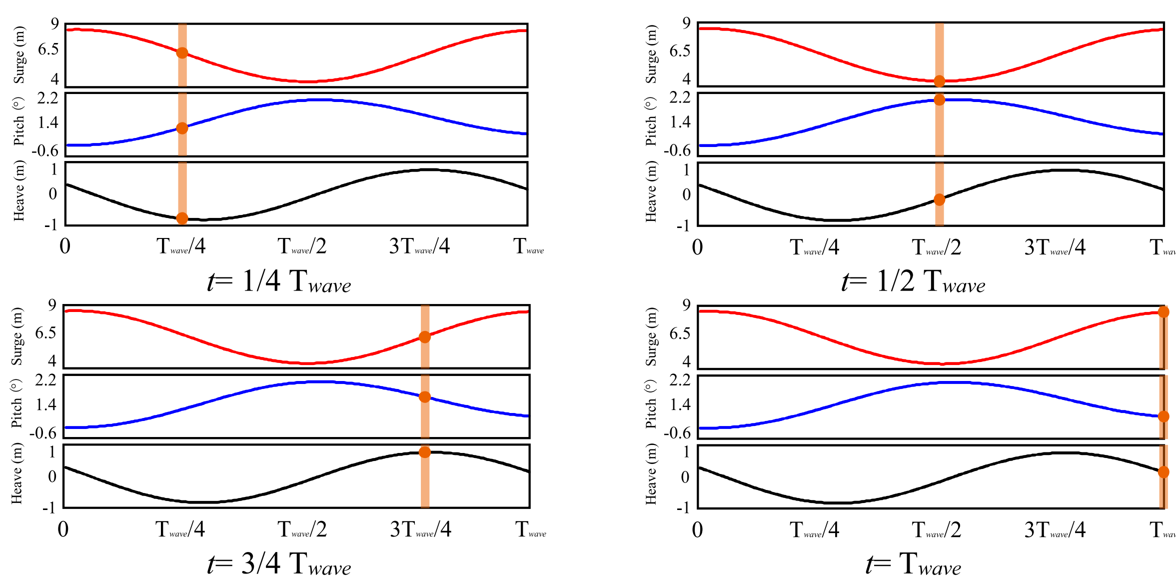

Fig. 20. Platform surge, heave, and pitch responses over one wave cycle: The four extracted phases correspond to the snapshots shown in Fig. 21.

typical Kármán vortex street (Pankanin et al., 2007). In contrast, the curved surface of the WHM chambers delays flow separation and generates a more continuous pressure-transition region around the platform. This helps mitigate the instantaneous impact of the incident waves and smooths the local dynamic-pressure gradient. At 1/2 T_{wave} (Fig. 21c and d), the platform pitch angle reaches its maximum. The separation region of the original platform moves upward toward the free surface. For the WHM configuration, the larger wave-contact area limits the

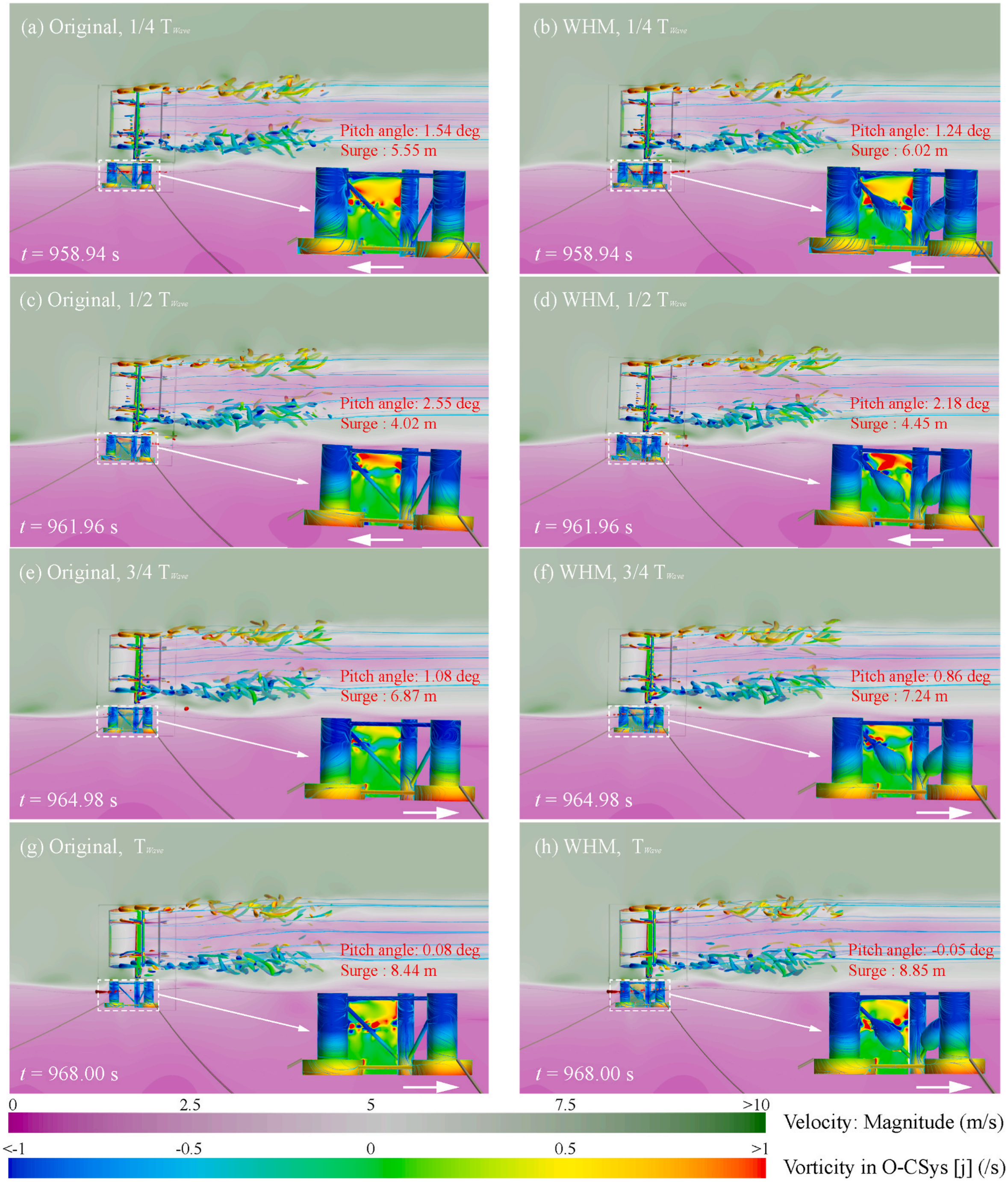

Fig. 21. Comparison of flow field patterns and near-platform vorticity between the original and WHM floating VAWTs during one wave cycle.

pitch amplitude, and large-scale vortical structures appear around the buoyancy chambers. The separation point remains near the upper connection between the chamber and the brace. During the second half of the wave cycle (from 1/2 T_{wave} to T_{wave}), the platform pitch angle gradually returns toward the neutral position as its motion becomes aligned with the wave direction. At 3/4 T_{wave} (Fig. 21e and f), recirculation regions appear near the braces in both configurations, while the WHM geometry causes stronger flow blockage and produces a more pronounced recirculation zone. At T_{wave} (Fig. 21g and h), the platform is ready to enter the next cycle. The original platform again exhibits symmetric vortex shedding near the braces, whereas the WHM configuration delays the separation point and disrupts the more periodic shedding rhythm seen in the original case. This behavior helps reduce fatigue loading and improve the overall stability of the system.

These flow mechanisms directly influence the unsteady aerodynamic loading transmitted to the rotor. To examine how this local flow regulation affects the overall dynamic response of the floating VAWT, the rotational energy histories of the two configurations are compared, as shown in Fig. 22.

In Fig. 22, the original floating VAWT experiences a strong fluctuation in rotational energy during the initial stage (0-150 s), with a peak value exceeding 2×10^6 J, followed by a decaying oscillatory response. In contrast, the WHM configuration exhibits a consistently restrained rotational behavior throughout the entire process. Its peak values remain below those of the original platform, and the mean rotational energy stays around 0.8×10^6 J, indicating a higher resistance to

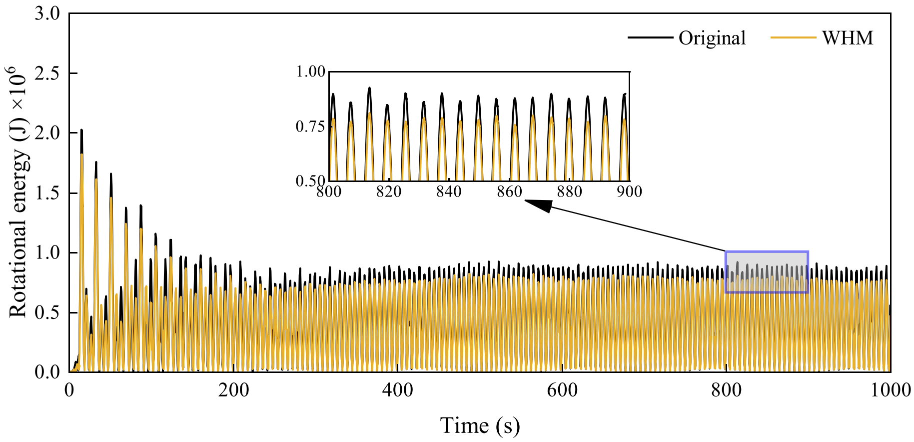

Fig. 22. Time history of rotational energy for the floating VAWT with and without the WHM structure.

external disturbances. During the steady-state stage (600-1000 s), the WHM case shows smaller fluctuation amplitudes and a more regular and symmetric waveform, as highlighted in the zoomed-in view of Fig. 22.

Please note that the VAWT has a highly symmetric rotor configuration, it is prone to yaw-pitch coupled oscillations under combined wind-wave excitation. The angular stability of the platform is therefore essential for ensuring safe system operation. The reduction in rotational energy and fluctuation amplitude achieved by the WHM buoyancy chambers demonstrates their potential to enhance angular stability and extend the service life of the floating VAWT system.

5.3.2. Coupled aero-hydro analysis

To clarify how the buoyancy chambers influence the aerodynamic load on the floating VAWT, the blade torque fluctuations are examined together with the platform motion responses, as shown in Fig. 23. Fig. 23a presents the torque curve of blade 1 over three steady rotor revolutions, while Figs. 23b and c display the surge and pitch motions of the floating VAWT over the same time interval. Only surge and pitch are included here because these two DOFs have the most direct impact on the relative inflow experienced by the blades.

In Fig. 23, both the original floating VAWT and the WHM-integrated configuration exhibit clear periodic torque fluctuations for blade B1 within one full revolution. However, noticeable differences appear in peak magnitude, phase evolution, and waveform smoothness. These variations stem from the azimuth-dependent aerodynamic behavior of the blade but are more directly governed by the coupled surge–pitch motions of the floating platform over the same time interval.

When the blade moves through the upwind region (0 to $T_1/3$), the angle of attack increases with azimuth. This strengthens the aerodynamic thrust and leads to a torque peak around $T_1/4$. At this moment, the platform moves in the negative X-direction (Fig. 23b), producing a superimposed inflow that further increases the effective relative velocity and raises the instantaneous torque. Fig. 23c shows that the WHM configuration exhibits a noticeably smaller pitch amplitude than the original platform. This pitch suppression keeps the effective inflow direction more stable and prevents the blade from deviating prematurely from the optimal angle-of-attack range. As a result, dynamic stall is delayed, producing a slightly higher torque peak compared with the original floating VAWT.

As the blade enters the transition zone before the downwind side ($T_1/3$ to $T_1/2$), the angle of attack gradually reduces, which weakens the aerodynamic thrust and results in the minimum torque value. On the downwind side ($T_1/2$ to T_1), blade B1 is affected by wake deficits generated by the upwind blades, which reduces the incoming velocity and results in a flatter torque response.

Once the blade passes the downwind zone (T_1 to $4T_1/3$), the platform gradually returns toward its equilibrium position, and the pitch angle

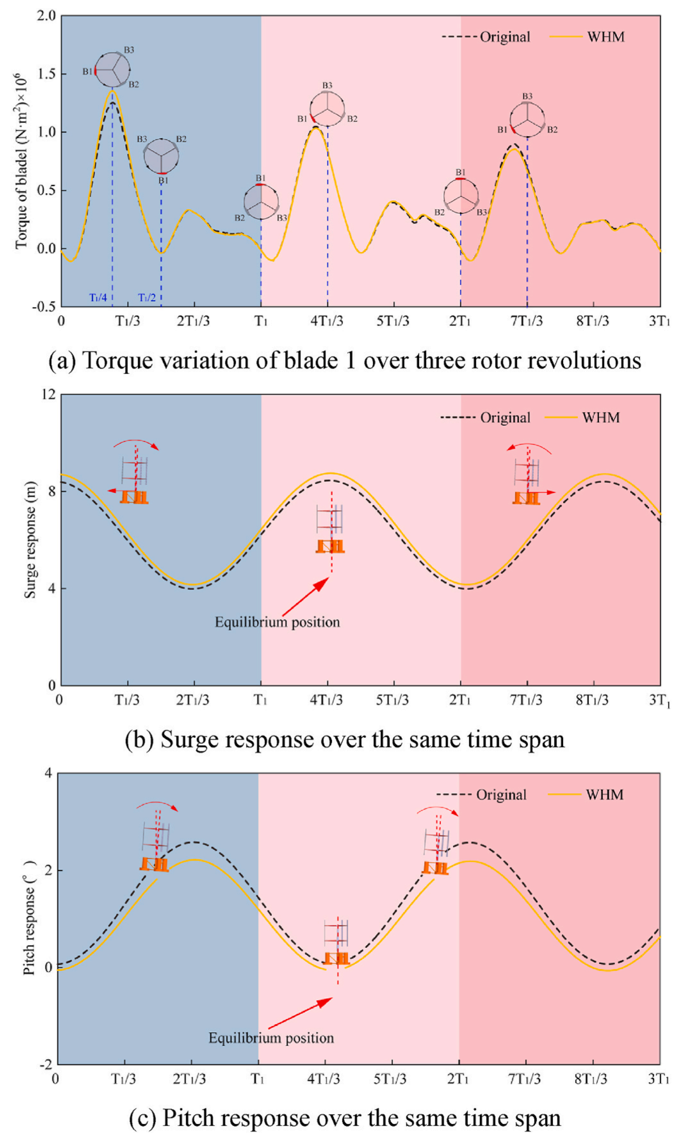

Fig. 23. Coupled response of blade torque and platform motion for the floating VAWT over three rotor revolutions.

approaches zero. The inflow disturbance caused by platform motion becomes much weaker, and the aerodynamic response is dominated by the intrinsic blade characteristics rather than aero-hydro coupling. Consequently, the torque curves of the two configurations become nearly identical, with their peaks almost fully overlapping.

As the blade moves into the third revolution and the platform shifts in the positive X-direction ($2T_1$ to $7T_1/3$), the effective inflow velocity decreases, which produces a gradual decay in torque amplitude. During this stage, pitch motion plays the dominant role in shaping the differences between the two configurations. Fig. 23c shows that the WHM design experiences a more moderated pitch variation due to enhanced damping. The slower pitch-recovery rate weakens the inflow-compensation effect, resulting in slightly lower torque peaks in the downwind region compared with the original case.

Overall, the WHM design optimizes the platform–flow interaction by reducing pitch amplitude and phase variation. This enhances torque peaks in the upwind region and suppresses high-frequency torque fluctuations across the full cycle. Although the WHM case exhibits slightly weaker inflow compensation in the downwind region, leading to marginally lower peaks, the overall periodic performance is smoother and more stable. This behavior helps reduce power-output variability and improves energy-conversion efficiency for the floating VAWT.

6. Conclusions

A bio-inspired semi-submersible platform was proposed to improve the hydrodynamic stability of floating VAWTs. Three biomimetic buoyancy-chamber configurations were developed using a Bézier-curve-based parametric design approach and systematically evaluated through fully coupled CFD simulations. Their hydrodynamic performance was first compared with the original OC4 platform and subsequently benchmarked against conventional buoyancy structures with equivalent volume. The optimal configuration was then integrated into a floating VAWT system to investigate its influence on coupled aero-hydrodynamic behavior. Based on the obtained results, the main conclusions are summarized as follows:

(1) The water hyacinth-inspired buoyancy chambers significantly improve the hydrodynamic performance of the semi-submersible platform by modifying the added-mass distribution, hydrodynamic damping, and buoyancy allocation. Compared with the original platform, all biomimetic configurations achieve noticeable reductions in the dominant heave and pitch responses while redistributing loads within the catenary mooring system. Among the three designs, the WHM configuration exhibits the most balanced performance in surge, heave, and pitch, providing an effective compromise between motion suppression and hydrodynamic stability. Although the tension in the wave-facing mooring line increases, all safety factors remain well above the API-RP-2SK requirement, confirming that the improved stability is achieved without compromising mooring safety.

(2) Comparison with conventional spherical, cylindrical, and disc-shaped buoyancy structures of equivalent volume demonstrates that the superior performance of the WHM configuration originates from its biomimetic geometry rather than buoyancy enhancement alone. The streamlined buoyancy chambers promote smoother flow attachment, weaken flow separation around the braces, and suppress unsteady vortex shedding, thereby enhancing hydrodynamic damping and reducing wave-induced platform motions. These flow-control characteristics provide a physical explanation for the improved stability of the biomimetic platform.

(3) When integrated into the complete floating VAWT system, the WHM platform maintains its hydrodynamic advantages and improves the coupled aero-hydrodynamic performance. Compared with the original system, the surge, heave, and pitch responses decrease by approximately 0.8%, 11%, and 10%, respectively. The improved platform stability provides more favorable inflow conditions for the rotor, resulting in reduced aerodynamic fluctuations and smoother power output. Although the mean power coefficient changes only slightly, the standard deviation of the power coefficient decreases by approximately 8%, demonstrating improved power-production stability and operational reliability.

The present study has several limitations that should be noted. To focus on the hydrodynamic effects of the biomimetic concept, both the floating platform and the VAWT rotor were modeled as rigid bodies, while the WH buoyancy chambers were represented using a uniform rigid plastic material. As a result, the potential influence of structural deformation, material flexibility, and fluid-structure interaction on the dynamic behavior of the biomimetic chambers was not considered. Future work will integrate finite element analysis with CFD simulations to investigate the structural responses of biomimetic chambers fabricated from different materials under wave loading. Particular attention will be given to geometric nonlinearities, stress concentrations, fatigue behavior, and aero-hydro-elastic coupling effects, with the aim of establishing more practical design guidelines for future biomimetic floating wind turbine platforms.

CRediT authorship contribution statement

Kunpeng Liu: Data curation, Formal analysis, Investigation, Methodology, Software, Validation, Writing – original draft. **Haoda Huang:** Data curation, Formal analysis, Methodology, Supervision, Writing – review & editing. **Qingsong Liu:** Formal analysis, Funding acquisition, Methodology, Project administration, Resources, Software, Supervision, Visualization, Writing – original draft, Writing – review & editing. **Qiang Zhang:** Methodology, Writing – review & editing. **Chun Li:** Funding acquisition, Methodology, Resources, Supervision, Validation, Writing – review & editing. **Gregorio Iglesias:** Formal analysis, Resources, Software, Writing – review & editing. **Jin Wang:** Resources, Writing – review & editing. **Musa Bashir:** Formal analysis, Funding acquisition, Resources, Writing – review & editing.

Declaration of competing interest

The authors declare that they have no known competing financial interests or personal relationships that could have appeared to influence the work reported in this paper.

Acknowledgements

This research is primarily supported by the SMARTBLADE project (Grant No. 101204880) funded by the European Commission under the Horizon Europe (Marie Skłodowska Curie Actions). Additional funding is provided by UKRI Innovate UK (TS/Y006364/1, TS/Y005236/1, TS/X018407/1), the National Key R&D Program of China (No. 2024YFA1012500) and the National Natural Science Foundation of China (No. 52376204). Computing support from Liverpool John Moores University and the University of Liverpool is also gratefully acknowledged.

Appendix A. Details of equivalent-volume benchmark buoyancy structures

To evaluate whether the observed performance improvements originate from the biomimetic geometry rather than buoyancy enhancement alone, three conventional buoyancy structures, namely cylindrical, spherical, and disc-shaped configurations, were introduced as benchmark cases. All conventional structures were designed to have the same buoyancy volume (2.025×10^4 m^3) as the WHM configuration and were installed at the center of the inclined braces.

Specifically, the cylindrical buoyancy structure was generated by extruding a circular section along the brace direction with a length of 16.038 m and a diameter of 6.443 m. The spherical structure had a diameter of 9.919 m, while the disc-shaped structure had a diameter of 12.281 m and a thickness of 4.360 m. The geometric arrangements of the four buoyancy configurations are shown in Fig. A1.

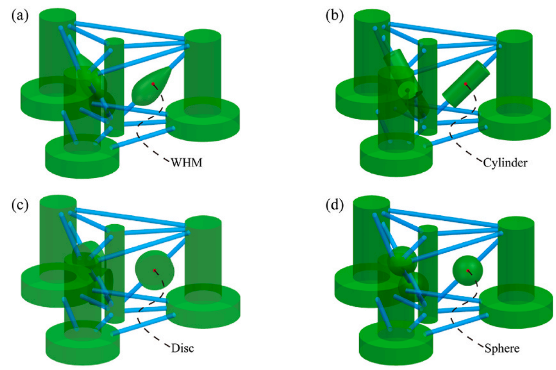

Fig. A1. Geometric configurations of equivalent-volume buoyancy structures: (a) WHM biomimetic chamber; (b) cylindrical structure; (c) disc-shaped structure; and (d) spherical structure.

The mass-related properties of the four configurations before ballast adjustment are summarized in Table A1. To ensure a fair hydrodynamic comparison, ballast water was subsequently adjusted so that all platforms maintained the same draft depth as the WHM platform. The resulting mass properties after ballast adjustment are presented in Table A2. As shown in Tables A1 and A2, the differences in total mass, center of gravity, and moments of inertia among the four configurations remain small, indicating that the comparison primarily reflects the influence of buoyancy geometry rather than differences in hydrostatic characteristics.

Table A1
Mass-related parameters of the equivalent-volume buoyancy structures without ballast water.

	Mass/kg	Center of mass/m (below the waterline)	I_{xx}/kg·m^2	I_{yy}/kg·m^2	I_{zz}/kg·m^2
WHM	4,693,156.00	−7.41	2.24×10^9	2.24×10^9	3.33×10^9
Cylinder	4,705,235.50	−7.39	2.24×10^9	2.24×10^9	3.33×10^9
Sphere	4,694,898.00	−7.40	2.24×10^9	2.24×10^9	3.33×10^9
Disc	4,704,890.00	−7.39	2.24×10^9	2.24×10^9	3.33×10^9

Table A2
Mass-related parameters of the equivalent-volume buoyancy structures after ballast adjustment.

	Mass/kg	Center of mass/m (below the waterline)	I_{xx}/kg·m^2	I_{yy}/kg·m^2	I_{zz}/kg·m^2
WHM	14149470.00	−13.42	6.79×10^9	6.79×10^9	1.18×10^{10}
Cylinder	13922952.00	−13.45	6.69×10^9	6.69×10^9	1.16×10^{10}
Sphere	13980785.00	−13.45	6.72×10^9	6.72×10^9	1.17×10^{10}
Disc	13922606.00	−13.45	6.69×10^9	6.69×10^9	1.16×10^{10}

To ensure that the hydrodynamic comparisons presented in Section 5.2 are not affected by mesh-resolution differences, all benchmark geometries were discretized using meshing strategies consistent with that adopted for the WHM platform. The same local refinement level was applied around the buoyancy structures and free-surface region, resulting in comparable mesh densities among the four configurations. The corresponding mesh information is summarized in Table A3.

Table A3
Mesh information of benchmark buoyancy structures

Parameter	WHM	Cylinder	Sphere	Disc
Grid size in WH region	0.2	0.2	0.2	0.2
Grid number of the individual platform	7,980,858	8,011,884	7,983,768	8,011,281

References

American Petroleum Institute, 2001. Design, Manufacture, Installation, and Maintenance of Synthetic Fiber Ropes for Offshore Mooring. Boston.

Battisti, L., Persico, G., Dossena, V., Paradiso, B., Raciti Castelli, M., Brighenti, A., Benini, E., 2018. Experimental benchmark data for H-shaped and troposkien VAWT architectures. Renew. Energy 125, 425–444.

Cao, F., Li, Y., Ning, D., Shi, H., Han, Z., 2025. Assessment of wind and wave energy resources and optimal site selection for joint development near the Shandong Peninsula. Ocean. Eng. 342.

Cheng, P., Huang, Y., Wan, D., 2019. A numerical model for fully coupled aero-hydrodynamic analysis of floating offshore wind turbine. Ocean. Eng. 173, 183–196.

Claessens, M.C., 2006. The Design and Testing of Airfoils for Application in Small Vertical Axis Wind Turbines. Delft University of Technology, Netherlands.

Cruz, DMd, Zangalli, L.B., Barreto, MdÁ., et al., 2024. Offshore mooring challenges for FOWT systems and MRE devices: synthetic fiber solutions for mooring ropes. Proceedings of the Roge Conference. Brazil.

Enterprise, S., 2022. Opportunit for Vertical Axis Wind Turbines in Floating Offshore Wind.

Ghigo, A., Faraggiana, E., Giorgi, G., Mattiazzo, G., Bracco, G., 2024. Floating vertical Axis Wind Turbines for offshore applications among potentialities and challenges: a review. Renew. Sustain. Energy Rev. 193.

GWEC, 2026. Global Wind Report 2026. Global Wind Energy Council (GWEC), Brussels, Belgium.

Han, Y., Le, C., Ding, H., et al., 2017. Stability and dynamic response analysis of a submerged tension leg platform for offshore wind turbines. Ocean. Eng. 129, 68–82.

He, L., Zhang, R., Yang, X., et al., 2025. Structural parameter optimization of a semi-submersible floating offshore wind turbine platform under typhoon conditions considering wind-wave interaction. Ocean. Eng. 335, 121717.

Hou, C.L., Yu, W., Chiang, M.H., et al., 2025. Stochastic model predictive control of a 10-MW semi-submersible floating offshore wind turbine: a comparative study with gain-scheduled PI, LQR and MPC controllers. Ocean. Eng. 340, 122431.

Johannesen, I.P., 2024. Enhancing Pitch Stability in Floating Wind Platforms: the Hydrodynamic Effects of Thin Plates. University Of Plymouth, England.

Li, D., Gao, Y., Chen, J., et al., 2025. Heave plate optimization for enhanced performance of semi-submersible wind turbines. Ships Offshore Struct. 20, 2545908.

Li, Y., Li, X., Ren, N., et al., 2022. Hydrodynamic responses of a novel modular floating structure System with multi-direction expansion. J. Offshore Mech. Arctic Eng. 145 (3), 030902.

Liao, L., Huang, Q., Wang, L., et al., 2025. Data-Driven load suppression and platform motion optimization for semi-submersible wind turbines. J. Mar. Sci. Eng. 13 (10), 1839.

Lin, C., Zhang, Q., Sheng, S., et al., 2025. Novel design and performance evaluation of a hybrid system of floating offshore wind turbine and Sharp-Eagle WECs. Ocean. Eng. 340, 122387.

Lin, T.-H., Yang, R.-Y., 2023. Stability analysis and environmental influence evaluation on a hybrid mooring System for a floating offshore wind turbine. J. Mar. Sci. Eng. 11 (12), 2236.

Liu, Q., Bashir, M., Huang, H., et al., 2025. Nature-inspired innovative platform designs for optimized performance of floating vertical Axis wind turbines. Appl. Energy 380, 125120.

Liu, Q., Bashir, M., Iglesias, G., et al., 2024. Investigation of aero-hydro-elastic-mooring behavior of a H-type floating vertical axis wind turbine using coupled CFD-FEM method. Appl. Energy 372, 123816.

Llamosas-Mayca, W.H., Hernández-Díaz, A.M., Pérez-Aracil, J., et al., 2025. Enhancing the shape-optimization of submerged arches using Bézier curves. Results Eng. 28, 108023.

López-Queija, J., Jugo, J., Tena, A., et al., 2024. Floating offshore wind turbine nonlinear model predictive control optimisation method. Ocean. Eng. 314, 119754.

National Renewable Energy Laboratory, 2014. Definition of the Semisubmersible Floating System for Phase II of OC4. NREL, United States.

NEW ATLAS, 2022. 1-MW floating vertical axis wind turbine to be deployed off Norway. https://newatlas.com/energy/seatwirl-vawt-norway/. (Accessed 28 May 2026).

offshoreWIND, 2025. Verti-Go Project Awarded EUR 15 Million for 2 MW Floating Vertical Axis Wind Turbine Demo. https://www.offshorewind.biz/2025/09/02/verti-go-project-awarded-eur-15-million-for-2-mw-floating-vertical-axis-wind-turbine-demo/. (Accessed 28 May 2026).

Pankanin, G.L., Kulińczak, A., Berliński, J., 2007. Investigations of Karman vortex street using flow visualization and image processing. Sensor Actuator Phys. 138 (2), 366–375.

Saeed, N., Gong, J., Wan, Y., et al., 2024. A novel design of multifunctional offshore floating platform structure based on topology optimization. Eng. Struct. 306, 117782.

Siemens Digital Industries Software, 2025. Simcenter STAR-CCM+ User Guide. Siemens. Version 2502.

Tian, H., 2025. Vibration Suppression of Floating Offshore Wind Turbines. Aalborg University, Denmark.

Tran, T.T., Kim, D.-H., 2016. Fully coupled aero-hydrodynamic analysis of a semi-submersible FOWT using a dynamic fluid body interaction approach. Renew. Energy 92, 244–261.

Ullah, F., Alam, M.M., 2026. State-of-the-art review of deep-sea wind turbine: installation, cost, instability, flow-induced oscillation, failure, maintenance, and power cost. Appl. Energy 408.

Yang, H., Tan, T., Ren, G., et al., 2025. The dual nature of water hyacinth (Pontederia crassipes): environmental threats and sustainable solutions. Water Biol. Secur. 4 (3), 100359.

Zhao, H., Wei, K., Yang, W., 2025. Further study of heave plate designs for enhancing motion control of floating offshore wind turbines. Ocean. Eng. 327, 121016.